

Towards near-unity β factor and collection efficiency in single-photon sources: employing dielectric rings to suppress the emission into radiation modes

Martin Arentoft Jacobsen,^{*a} Luca Vannucci,^a Julien Claudon^b, Jean-Michel Gérard,^b and Niels Gregersen^a

In this paper, we demonstrate that a few-period circular Bragg reflector around an infinite nanowire can increase the β factor of the fundamental mode up to 0.999 due to further suppression of the emission into radiation modes caused by a photonic band gap effect. We then apply this strategy in the practically relevant case of the finite-sized SPS based on tapered nanowires and demonstrate that the collection efficiency can be further increased. Additionally, we also show the beneficial effects of adding optimized high-index rings around the micropillar SPS.

Date: 06/07/2023

1 Introduction

The quantum optics community is in hot pursuit of designing, developing and fabricating deterministic sources of single indistinguishable photons^{1–4} and entangled photon pairs⁵ as such sources are crucial key building blocks in scalable quantum technologies^{6,7}. One of the main figures of merit of the single-photon source (SPS) is the collection efficiency, ϵ , defined as the number of collected photons in the desired out-coupling channel relative to the number of emitted photons from the source. The success probability of any N multi-photon interference experiment is namely proportional to the collection efficiency and scales as $P \propto \epsilon^N$. Thus it is of great importance to increase ϵ towards unity. One of the main approaches towards the development of SPSs is based upon quantum dots (QDs)^{1,2,8–11} embedded in carefully engineered photonic nanostructures^{3,4,12}. The discrete energy levels of the QD and the large magnitude of the Coulomb interaction between trapped charge carriers allow for deterministic emission of single photons through the spontaneous emission process, while the design of the photonic nanostructure aims at optimizing the collection of the photons.

A main design strategy for the photonic nanostructures is to build a cavity around the QD and exploit cavity quantum electrodynamics (CQED) in the weak coupling regime and thereby making use of the Purcell effect¹³ to enhance the emission into the optical mode of interest, typically the fundamental cavity mode. The enhancement is quantified by the Purcell factor¹⁴, $F_p = \Gamma_C/\Gamma_0$, where Γ_C is the emission rate into the cavity mode and Γ_0 is the emission rate in a bulk medium. The β factor then quantifies how much of the total emission is funneled into the cavity mode¹²:

$$\beta = \frac{\Gamma_C}{\Gamma_T} = \frac{F_p}{F_p + \Gamma_B/\Gamma_0}, \quad (1)$$

where Γ_T is the total emission rate and Γ_B is the emission rate into all other background modes. For SPS designs with large Purcell enhancement, a single-mode model^{15–17} (SMM) is typically

accurate at describing the collection efficiency, $\epsilon_{SMM} = \gamma\beta$, where γ (the transmission coefficient) is the ratio between the collected light of the cavity mode in the out-coupling channel and the emission into the cavity mode. As such it is also important that the design ensures γ approaching unity. Relying on Purcell enhancement to obtain good collection efficiency results in narrow-band designs, requiring careful spectral alignment between the QD and the cavity¹⁸. Still, this design approach has so far resulted in the most successful SPSs such as the micropillar cavity^{17–21} and the open cavity approach²² demonstrating up to $\epsilon \sim 0.6$ into a first lens²⁰ and into a fiber²², respectively, combined with highly indistinguishable photon emission. However, still increasing the Purcell factor further towards the strong-coupling regime will reduce the indistinguishability due to phonon induced decoherence leading to a trade-off between the collection efficiency and the indistinguishability²³. It has then been shown that this trade-off can be circumvented by suppressing the background emission, Γ_B , allowing for simultaneous increase of the collection efficiency and the indistinguishability²⁴. Still, the "hourglass" design in Ref.²⁴ benefited from resonant cavity effects such that the Purcell enhancement was combined with the suppression effect. There are also several broadband designs which aim at controlling and suppressing the background emission, Γ_B , hereby obtaining large β factors and thus high collection efficiency in a broad spectral range. These designs include the photonic nanowire^{16,25–28} and the photonic crystal waveguide^{29–34}. Other broadband designs include the circular Bragg grating or "bullseye" cavity^{20,35–41}.

In the quest for near unity β factor and collection efficiency, we explore the introduction of few-period (1-3) circular Bragg reflectors around nanowires or micropillars, in an attempt to decrease the spontaneous emission (SE) rate into background modes, Γ_B . The circular Bragg reflector consists of alternating layers of air and high-index materials thus forming cylindrical rings separated by air gaps. In this paper, we will provide a detailed physical description of how cylindrical rings around an infinite nanowire can influence the emission into radiation modes referring to established literature^{42–51}. We will then demonstrate how the few-period circular Bragg reflector around an infinite nanowire can increase the β factor of the fundamental mode ($\beta = \Gamma_{HE_{11}}/\Gamma_T$) up to 0.999 due to further suppression of the emission into radiation

^a DTU Electro, Department of Electrical and Photonics Engineering, Technical University of Denmark, DK-2800 Kongens Lyngby, Denmark. E-mail: maaja@dtu.dk

^b Univ. Grenoble Alpes, CEA, Grenoble INP, IRIG, PHELIQS, “Nanophysique et Semiconducteurs” Group, F-38000 Grenoble, France.

modes caused by a photonic band gap effect. Finally, we will apply this strategy in the practically relevant case of the finite-sized SPS based on tapered nanowires sketched in Figs. (1a-1b). Additionally, we also show the beneficial effects of adding optimized high-index rings around micropillars as shown in Fig. (1c).

This paper is organized as follows: in Sec. (2), we present our theoretical framework based on the Fourier modal method and a novel analytical method. In Sec. (3), we describe the physics of the circular Bragg reflector. Subsequently, we use the analytical method to present and analyze the emission rates in the infinite nanowire (Sec. (4)) and in the infinite nanowire with rings (Sec. (5)). In Sec. (5), we also present the optimization of the β factor. In Sec. (6) and Sec. (7), we present the photonic nanowire SPS with rings and the micropillar SPS with rings respectively.

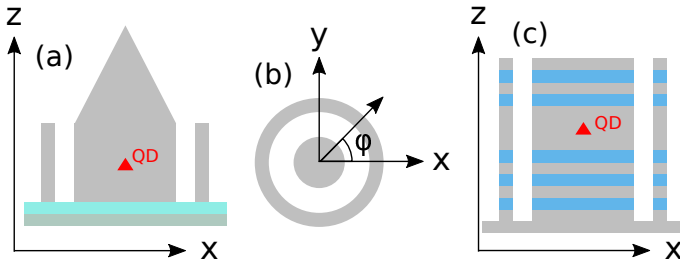


Fig. 1 (a) Sketch of the photonic nanowire SPS with a needle tapering surrounded by 1 ring. (b) Cross sectional view of the nanowire with 1 ring. (c) Sketch of the micropillar SPS surrounded by 1 ring. The cross sectional view of the micropillar is similar to the nanowire.

2 Theory

To calculate the figures of merit we compute the total and collected power from the source by solving Maxwell's equations in the frequency domain, modeling the QD as a classical point dipole. Within the dipole approximation, the emission rate of the QD can namely be related to the classical emitted power of a dipole using the following relationship $\Gamma/\Gamma_0 = P/P_0$ ⁵², where P is the emitted power of the dipole and P_0 is the power emitted in a bulk medium. The β factor is then defined as $\beta = P_{\text{mode}}/P_{\text{T}}$, where P_{mode} is the power emitted into our mode of interest (for instance the cavity mode or the fundamental mode) and P_{T} is the total emitted power. The collection efficiency is then defined as $\epsilon_g = P_{\text{collected},g}/P_{\text{T}}$, where $P_{\text{collected},g}$ is the power collected in the far-field of a lens with numerical aperture NA taking into account the overlap with a Gaussian shaped field profile¹⁷.

All structures considered in this paper feature cylindrical symmetry. The current distribution of the point dipole is given by: $\mathbf{J}(\mathbf{r}) = -i\omega\mathbf{p}\delta(\mathbf{r} - \mathbf{r}_d)$, where ω is the frequency, \mathbf{r}_d is the position of the QD and \mathbf{p} is the dipole moment. We assume that dipole is placed on-axis and the dipole orientation is in-plane. We expand the generated field upon the eigenmodes of the structure which consist of a finite set of guided modes and a continuum of radiation⁵³. For the finite sized structures, the structure is split into layers with uniform refractive index along the z-direction and in each layer the field is expanded upon the eigenmodes. The expression for the electrical field is then given by:

$$\mathbf{E}^{\pm}(r, \phi, z) = \sum_{n=1}^N a_n^{\pm} \mathbf{e}_n^{\pm}(r, \phi) \exp(\pm i\beta_n z) + \sum_{s=1}^2 \int_0^{\infty} a_s^{\pm}(k_{\perp}) \mathbf{e}_s^{\pm}(r, \phi, k_{\perp}) \exp(\pm i\beta(k_{\perp})z) dk_{\perp}, \quad (2)$$

where \pm refers to forward or backwards propagation, β_n and $\beta(k_{\perp})$ are the propagation constants (not to be confused with the β factor), $\mathbf{e}(r, \phi)$ is the mode profile, a is the expansion coefficient, N is the total number of guided modes, k_{\perp} is the in-plane k -value and s refers to the two orthogonal solutions for the radiation modes. The guided modes are confined to regions with high refractive index, usually the core of the structure, and decay in regions with low refractive index such as air regions. Their propagation constant, β_n , satisfy the following relation $n_{\text{max}}k_0 \geq \beta_n > n_{\text{air}}k_0$, where $k_0 = 2\pi/\lambda_0$ is the free-space k -vector (λ_0 being the free-space wavelength) and we assume that the surrounding background material is air. The propagation constant of the radiation modes is related to the in-plane k -value: $\beta(k_{\perp}) = \sqrt{(n_{\text{air}}k_0)^2 - k_{\perp}^2}$. The radiation modes can be viewed as perturbed versions of the modes in a homogeneous air medium and are generally not confined to any specific regions. The continuum of radiation modes can be split into two parts namely the propagating radiation modes, $n_{\text{air}}k_0 \geq \beta(k_{\perp}) > 0$, and the evanescent radiation modes, $0 > \beta(k_{\perp})$. For the propagating radiation modes, the propagation constant also defines the angle of propagation with respect to the z-axis: $\beta = k_0 \cos(\theta)$ (with $n_{\text{air}} = 1$), which is sketched in Fig. (2). All the eigenmodes in Eq. (2)

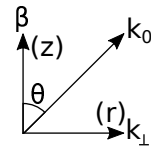


Fig. 2 Sketch of the relation between the propagation constant, β , and the in-plane k -component, k_{\perp} , for the propagating radiation modes. β also defines the angle of propagation with respect to the z-axis, $\beta = k_0 \cos(\theta)$.

have angular momentum of $m = 1$ as the dipole is placed on-axis and has in-plane orientation and thus only couples to modes with $m = 1$ (all other modes have in-plane electrical field components of zero at $r = 0$). The expansion coefficients can be derived from Lorentz reciprocity theorem^{53,54} and the expressions are given in supplementary (10.6). The emitted power can then be evaluated⁵²:

$$P = -\frac{1}{2} \int_V \text{Re}[\mathbf{J}^*(\mathbf{r}) \cdot \mathbf{E}(\mathbf{r})] dV = \frac{\omega}{2} \text{Im}[\mathbf{p} \cdot \mathbf{E}(\mathbf{r}_d)]. \quad (3)$$

The resulting expressions for the power are also given in supplementary (10.6). In the infinite structures, the evanescent modes do not contribute to the power and thus one can replace the integral over all k_{\perp} in Eq. (2) with $\int_0^{k_0}$. The total emitted power in an infinite structure can then be written as:

$$P_T = \sum_{n=1}^N P_{g,n} + \sum_{s=1}^2 \int_0^{k_0} p_s(k_\perp) dk_\perp = P_G + P_R, \quad (4)$$

where the first term corresponds to the power into the guided modes and the second term to the power into radiation modes. We choose an orthogonalization, s , such that $p_1(k_\perp) = 0$ and often we will simply use $p(k_\perp) = p_1(k_\perp) + p_2(k_\perp)$, where $p(k_\perp)$ is the power spectrum for the radiation modes.

We have developed and used a novel method for the infinitely extending structures to analytically construct the radiation modes of a multi-layered cylindrical structure inspired by previous work^{53,55-66}. This method allows for direct insight and efficient calculations. The method is described in supplementary (10.1&10.4) and along with the guided modes of a multi-layered cylindrical structure (supplementary 10.5). For the finite-sized structures we make use of a numerical method which also allows access to all the modes and this method is also described in supplementary (10.1).

3 Suppression of the spontaneous emission into radiation modes using a circular Bragg reflector

Multi-layered cylindrical structures have been considered in view of applications such as lasers⁶⁷⁻⁷², fibers^{55,73-76} and sensing⁷⁷, in addition to SPSs, and their physics have been described for instance in Refs.⁴²⁻⁵¹. Just as plane waves are reflected at an interface between two materials, so are cylindrical waves; however, the main key property of cylindrically propagating waves, which are given by the Bessel functions of the first and second kind, $J_m(k_\perp r)$ and $Y_m(k_\perp r)$, is that they are non-periodic which also leads to reflections being radius dependent. This means that the typical argument for $\lambda_{\text{eff}}/4$ thicknesses used in planar structures when creating a photonic band gap for plane waves is no longer valid. Instead, the dimensions of each individual ring and each air gap should all be free parameters and the optimized parameters are also influenced by the total numbers of rings. However, for sufficiently large radii and/or in-plane k -components the cylindrical waves approach the periodic behavior of plane waves. Ultimately, different expressions can be found, which are to either be minimized/maximized in order for instance to achieve maximum or minimum reflection or create a horizontal cavity for a specific value of k_\perp . Maximizing the reflection will then lead to a photonic band gap. However, our goal is to increase the β factor by suppressing the emission into radiation modes, Γ_R , which consist of a continuum of cylindrically propagating waves with $k_\perp \in [0, k_0]$. We thus need to take into account all the possible values of k_\perp , but translating this into a wavelength interval would result in an infinitely broad range. Fortunately, the k_\perp depends on the refractive index of the material, n_{mat} , and k_\perp inside a material is given by: $k_{\perp,\text{mat}} = \sqrt{k_\perp^2 + (n_{\text{mat}}^2 - 1)k_0^2}$, such that $k_{\perp,\text{mat}} \in [\sqrt{(n_{\text{mat}}^2 - 1)k_0^2}, n_{\text{mat}}k_0]$ and here the Bessel functions take the arguments $J_m(k_{\perp,\text{mat}}r)$ and $Y_m(k_{\perp,\text{mat}}r)$. Thus, a high refractive index contrast effectively reduces the required width of the photonic band gap, while simultaneously increasing the reflection and the width of the photonic band gap. However, the reflected

wave must not provide constructive interference at the position of the QD hereby creating a cavity, but this will be taken into account in the optimization.

To support these general considerations, we will make use of an example and consider an infinitely long wire consisting of GaAs with a diameter, $D = 300\text{nm}$, and then we add 1 and 2 rings. We use a wavelength of $\lambda_0 = 895\text{nm}$ throughout the paper, and the refractive index of GaAs is set to be: $n_{\text{GaAs}} = 3.5015$. The in-plane cross-sectional view of the wire with 0, 1 and 2 rings is shown in Figs. (3a-3c) with the dimensions being indicated. We then select the radiation mode with $k_\perp = 0.5k_0$ and optimize the ring(s) dimensions to minimize $p(k_\perp = 0.5k_0)$.

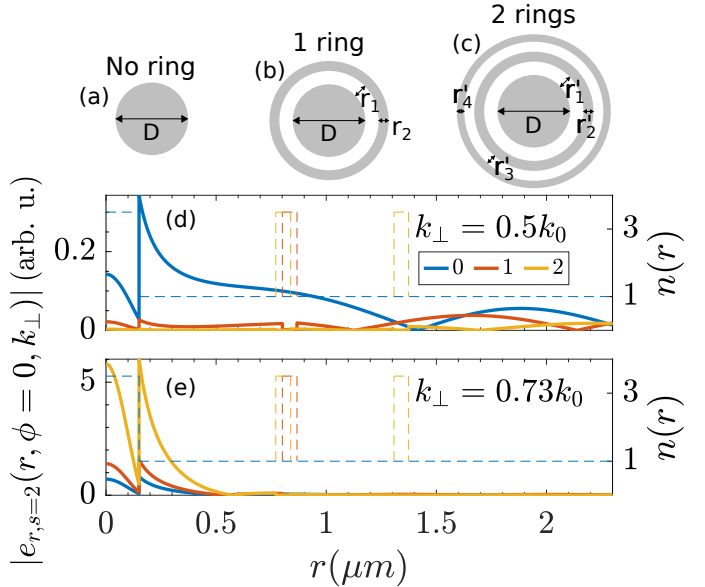


Fig. 3 Cross-sectional view of the wire with 0 (a), 1 (b) and 2 rings (c). The absolute value of the radial electrical field component (full lines) for the radiation mode with $k_\perp = 0.5k_0$ (d) and $k_\perp = 0.73k_0$ (e) is shown as a function of the radius, r , for 0, 1 and 2 ring(s). The dashed lines indicate the refractive index profile according to the right vertical axis. The color also indicates the numbers of rings and their position.

In Fig. (3d), the absolute value of the radial electrical field component for the radiation mode with $k_\perp = 0.5k_0$ is shown as a function of the radius, r , for 0, 1 and 2 ring(s). Here the electrical field is strongly suppressed at $r = 0$ for 1 ring and even more for 2 rings. The refractive index profile is also shown along with the field and the optimized ring parameters for 1 ring are given by: $r_1 = 650.7\text{nm}$ and $r_2 = 66.6\text{nm}$. For 2 rings: $r'_1 = 621.1\text{nm}$, $r'_2 = 67.2\text{nm}$, $r'_3 = 469.4\text{nm}$ and $r'_4 = 66.1\text{nm}$. This also shows that adding an extra ring can change the optimal dimensions of the first ring. However, minimizing $p(k_\perp = 0.5k_0)$ does not ensure that $p(k_\perp)$ is reduced for all values of k_\perp and in Fig. (3e), the field is shown for the radiation mode with $k_\perp = 0.73k_0$ and here the field is actually enhanced at $r = 0$ and thus $p(k_\perp = 0.73k_0)$ is increased. This shows the importance of considering the entire continuum and not just one value of k_\perp .

We can not solely focus on Γ_R when optimizing the β factor, as it also depends on both $\Gamma_{\text{HE}_{11}}$ and Γ_G , i.e., $\beta = \Gamma_{\text{HE}_{11}}/(\Gamma_R + \Gamma_G)$, where $\Gamma_{\text{HE}_{11}}$ is also included in the total SE for the guided modes

Γ_G . The rings can namely also influence the guided modes, however, the physics of the guided modes is different from the radiation modes as they are not propagating waves in the radial direction. In the low index air regions, they are instead described by the modified Bessel functions of $K_m(k_{\perp,g}r)$ and $I_m(k_{\perp,g}r)$, where $k_{\perp,g}$ is the in-plane k component of the guided mode (in the outer air region only $K_m(k_{\perp,g}r)$). If the ring is close enough to the central wire and reaches the evanescent tails of the guided modes, the emission rates will then be influenced. In Fig. (4a), the ab-

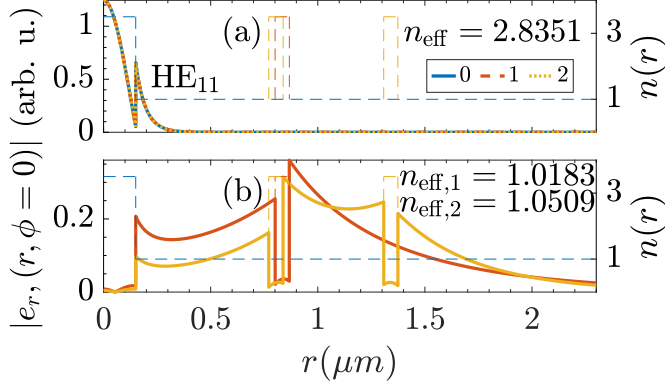


Fig. 4 (a) The absolute value of the radial electrical field component for the fundamental mode is shown as a function of the radius, r , for 0 (full line), 1 (dashed line) and 2 (dotted line) rings. The refractive index is indicated with the dashed lines as in Figs. (3d-3e). (b) The field for two selected guided modes for 1 and 2 rings respectively. The effective indices are indicated in the figures.

solute value of the radial electrical field component for the fundamental mode is shown as a function of the radius, r , for 0, 1 and 2 ring(s) with $D = 300\text{nm}$ and the exact same parameters obtained from the minimization of $p(k_{\perp} = 0.5k_0)$. Here the field of the fundamental mode is not influenced at all as the rings are too far away. However, in Fig. (4b), the field is shown for two new higher order guided modes which appear due to the rings. These are weakly confined ring modes and a small part of the field extends to the wire axis; as a result, rings can influence the SE rate into guided modes. Therefore, the optimization should not focus only on reducing Γ_R , and in the following we will use β as the objective function to be maximized.

4 Infinitely long nanowire

The starting point of the optimization is the bare nanowire for which we will then add rings. In this section, we will therefore present the normalized emission rates of a QD with an emission wavelength of $\lambda_0 = 895\text{nm}$ placed on-axis of an infinitely long GaAs nanowire without any rings. A sketch of the nanowire with an embedded QD is shown in Fig. (5a) and the cross-sectional view in Fig. (5b).

In Fig. (5c) the emission rates into the guided modes, the radiation modes and their sum is shown as a function of the wire diameter, D . For the smallest diameters all emission is suppressed as the fundamental mode is weakly confined and the emission into the radiation modes is suppressed due to the dielectric screening effect^{25,27}. Then the power into the fundamental mode rapidly

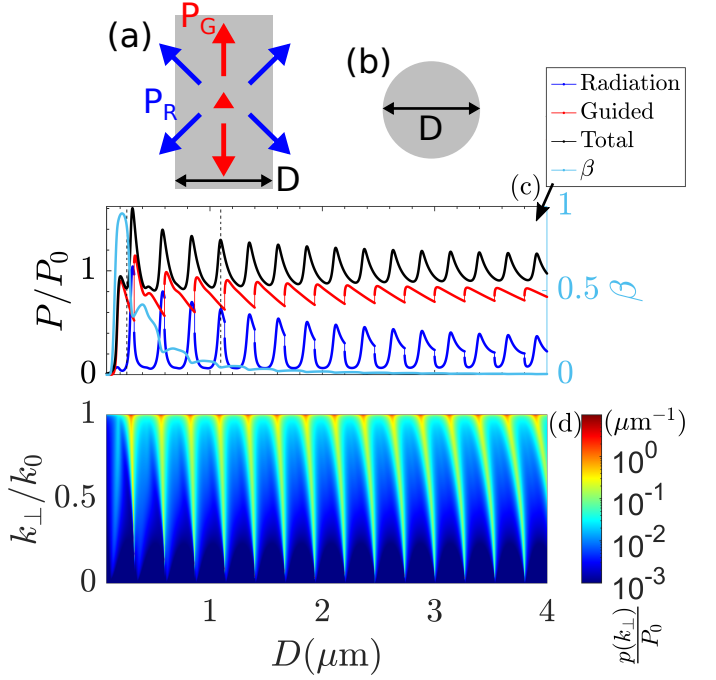


Fig. 5 (a) Sketch of the infinite nanowire with diameter, D , with a QD in the center. (b) Cross sectional view of the infinite nanowire. (c) P/P_0 as a function of D for the radiation modes, the guided modes, and their sum. The β factor (right y-axis) is also shown as a function of D . The vertical black dotted lines correspond to the diameters used in Fig. (6). (d) The spectrum $p(k_{\perp})/P_0$ as a function of D and k_{\perp}/k_0 .

increases as the confinement of the mode increases and thus also the electrical field at the center of the wire, whereas the emission into the radiation modes is still suppressed due to the dielectric screening effect. This is also the region, where the β factor (right y-axis in Fig. (5c)) is the largest and reaches a value of $\beta_{HE_{11}} = 0.9581$ at $D = 0.218\mu\text{m}$. As the diameter increases, the emission into the fundamental mode decreases due to the decreased confinement and field strength and so does the β factor. Furthermore, more guided modes appear and they appear in pairs where the $EH_{1,n}$ modes provide a discontinuous increase in the SE rate, quickly peak and then decrease, whereas the SE rate contribution from the $HE_{1,n+1}$ modes increase more slowly and then decrease⁷⁸. The emission into radiation modes follows a semi-periodic pattern with peaks and valleys, where the peaks increase in width and decrease in intensity as the diameter increases. These peaks also correspond to the peaks in the total emission and at these peaks there will also be dips in the β factor. Furthermore, there are discontinuous decreases exactly when the new guided modes appear such that the total emission rate is continuous, which showcases the transition between the radiation modes and the guided modes.

To understand the behavior of the emission into radiation modes we need to consider the spectrum $p(k_{\perp})/P_0$ which is shown in Fig. (5d) as a function of the wire diameter. Here we observe peak lines for k_{\perp} as a function of the diameter and these lines slowly start to bend as the diameter increases. The bending of these peak lines causes the peaks in P_R to increase in width and decrease in intensity. The reason for why the lines bend is found

by considering the behavior of each radiation mode. Each radiation mode namely experiences a reflection at the interface between the wire and the air which leads to interference between the outgoing and reflected wave at the position of the dipole, i.e., there can both be constructive and destructive interference leading to either increased or decreased emission. Therefore the emission into each radiation mode has peaks and valleys as a function of the diameter. For small diameters the period between the peaks is non-periodic due to the cylindrical nature of the modes and then approach a periodic behaviour for larger diameters. Nonetheless, the period between the peaks is determined by $k_{\perp,\text{GaAs}}$, and for the smallest diameters, these peaks almost overlap for all values of $k_{\perp,\text{GaAs}}$, but then they shift apart for increased diameters due to the different periods, which explains the bending in Fig. (5d). As such, the entire spectrum of $p(k_{\perp})/P_0$, which we wish to minimize in order to increase the β factor, will never become truly periodic.

5 Rings

We are now equipped to understand the influence of adding rings around the nanowire. A sketch of the infinite nanowire with a ring can be seen in Figs. (6a-6b). First, we consider two examples with one ring, where the diameter is fixed and the air gap, r_1 , and the ring thickness, r_2 , are varied.

In Figs. (6c-6h) the normalized emission into the guided modes P_G/P_0 , into radiation modes P_R/P_0 , and the $\beta_{\text{HE}_{11}}$ factor are shown as a function of the air gap, r_1 , and ring thickness, r_2 , for two selected diameters of $D_1 = 0.26\mu\text{m}$ and $D_2 = 1.0962\mu\text{m}$, both indicated by the vertical dotted lines in Fig. (5c). These diameters correspond to drastically different situations: for D_1 , the emission into radiation modes is very weak and the emission into the fundamental mode is large, while for D_2 , the emission into radiation modes is strong and the emission into the fundamental mode is weak. For the guided modes in Figs. (6c-6d), it can immediately be observed that the ring needs to be close to the central wire to influence the emission rate. This is exactly due to the evanescent field outside the center wire for the guided modes. It is the higher order modes with the smallest propagation constants which are responsible for the tails of slightly larger values of r_1 seen in Figs. (6c) and (6d). These modes namely decay the slowest outside the center wire. Additionally, weakly confined ring modes close to the wire can also influence the emission rate as discussed earlier. For the radiation modes, shown in Figs. (6e) and (6f), the rates are influenced in the entire parameter space and a semi-periodic interference pattern can be seen as a function of r_1 and r_2 , where the periods are much shorter for r_2 due to the large refractive index of GaAs. The strongest effects are observed within the first period of varying the air gap and ring thickness, i.e., here the maximum in $\beta_{\text{HE}_{11}}$ is found indicated by the magenta crosses and the minimum in P_R/P_0 indicated by the green pluses. For $D_1 = 0.26\mu\text{m}$, the magenta cross and green plus overlap exactly, which demonstrates that the β improvement results from inhibition of SE into radiation modes. For $D_2 = 1.0962\mu\text{m}$ there is a slight difference in the position of the magenta cross and green plus due to the SE contribution of the guided modes. For $D_1 = 0.26\mu\text{m}$ there is an increase in $\beta_{\text{HE}_{11}}$ from $\beta_{\text{HE}_{11}} = 0.8785$

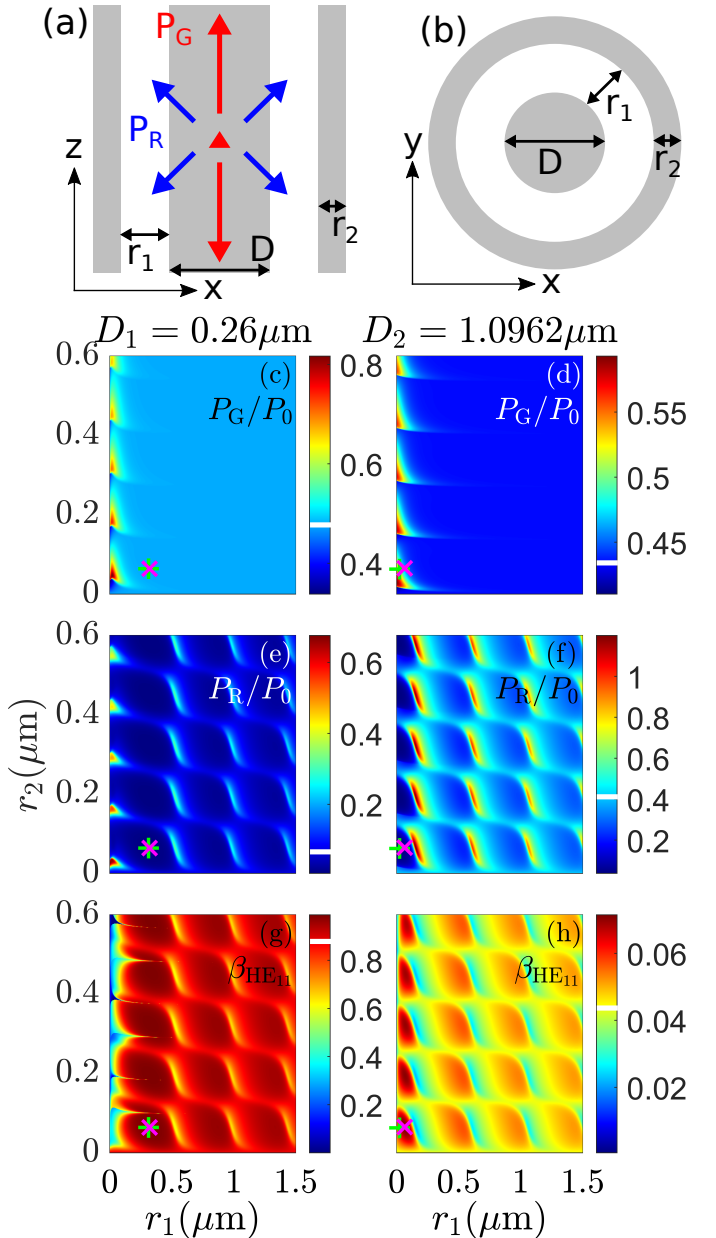


Fig. 6 Sketch of the infinite nanowire with one ring. There are two views of the cross-section, one for the z-x plane (a) and the y-x plane (b). The red triangle is the QD and the grey color signifies the GaAs. The center nanowire has diameter, D , the air gap is r_1 and the ring thickness is r_2 . (c-h) P_G/P_0 , P_R/P_0 and $\beta_{\text{HE}_{11}}$ as a function of the air gap, r_1 and ring thickness, r_2 for two selected diameters of $D_1 = 0.26\mu\text{m}$ and $D_2 = 1.0962\mu\text{m}$. Moving along the vertical axis for $r_1 = 0\mu\text{m}$ simply corresponds to increasing the diameter of the infinite nanowire. The white line in the color bars indicates the value of the wire without any rings. The green pluses correspond to the minimum of the emission into radiation modes, while the magenta crosses correspond to the maximum of the β factor.

to $\beta_{\text{HE}_{11,1\text{ring}}} = 0.9890$ and for $D_2 = 1.0962\mu\text{m}$ from $\beta_{\text{HE}_{11}} = 0.0437$ to $\beta_{\text{HE}_{11,1\text{ring}}} = 0.0715$. For the smaller diameter the absolute increase in $\beta_{\text{HE}_{11}}$ is larger as the dominating contribution to the background emission is P_R/P_0 which the ring can significantly reduce. Thus, already for one ring the effect of the photonic band gap can be observed. For the larger diameter, the emission into

higher order guided modes contribute significantly to the background emission which the ring does not control and therefore the absolute increase in $\beta_{\text{HE}_{11}}$ is not as large. We will nevertheless highlight in section (7), its beneficial effect for the performance of QD-micropillar SPS.

5.1 β factor optimization

We will now perform an optimization of the β factor (of the fundamental mode) as a function of the center diameter with respect to the ring dimensions. For one ring, the optimization is straight forward as the parameters of r_1 and r_2 can simply be scanned for each diameter as the computation is very fast due to the analytical method.

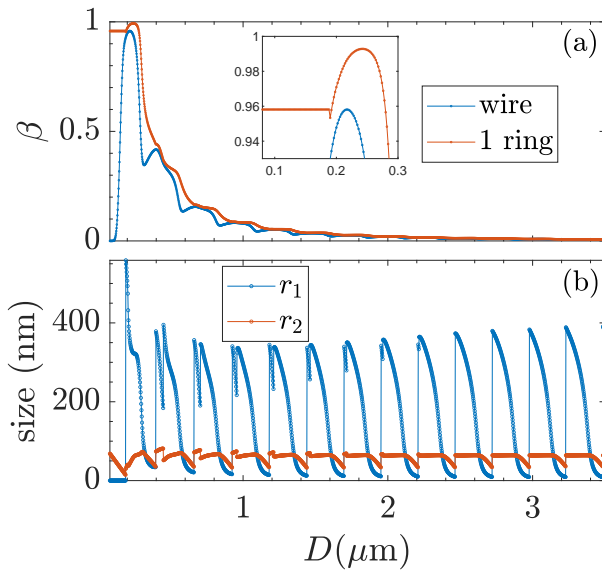


Fig. 7 (a) β factor as a function of the diameter for the wire and the wire with one optimized ring. (b) Optimized air gap, r_1 , and ring thickness, r_2 , as a function of the diameter.

In Fig. (7a) the β factor for the wire without rings and the wire with one optimized ring is shown as a function of the wire diameter. It is possible to increase the β factor for all diameters and a significant increase in the maximum β factor from $\beta_{\text{wire}} = 0.9581$ at $D = 0.218 \mu\text{m}$ to $\beta_{1\text{ring}} = 0.9928$ at $D = 0.242 \mu\text{m}$ with $r_1 = 323.37 \text{ nm}$ and $r_2 = 59.03 \text{ nm}$. As such the losses to other modes have been reduced from loss = 1 – 0.9581 = 0.0419 to loss = 1 – 0.9928 = 0.0072 such that the fraction of power lost is reduced by a factor 5.8. In Fig. (7b), the optimized parameters for the air gap and ring thickness are shown as a function of the wire diameter. For the smallest diameters the β factor is constant for the wire with 1 ring since the optimization basically increased the diameter as the air gap is 0 as seen in Fig. (7b). Generally, the optimized parameters follow a semi-periodic pattern, where the air gap features the largest changes compared to the ring thickness due to the difference in the refractive index between the GaAs and air. The optimized parameters deviate most from the periodic pattern for the smallest diameters where the non-periodic nature of the radiation modes due to the cylindrical

symmetry is more pronounced.

We will now also perform the optimization of the β factor for the two configurations of two and three rings around the wire, where we focus on the small diameter regime. For each configuration, we perform (i) one calculation where all air gaps and ring thicknesses are treated as free parameters, and (ii) another one where all air gaps and ring thicknesses are respectively identical (which we will call "fixed" in the following). In the former case we thus have $2N$ free parameters (with N being the numbers of rings) for a fixed diameter, while the second case only has 2 parameters. Details on the numerical optimization are given in supplementary (10.7&10.8). As discussed earlier it is important that all associated ring parameters are free when optimizing the β factor, however, we also wish to compare with fixed air gaps and ring thicknesses as this is typically used for other SPS design with cylindrical rings like the bullseye SPS.

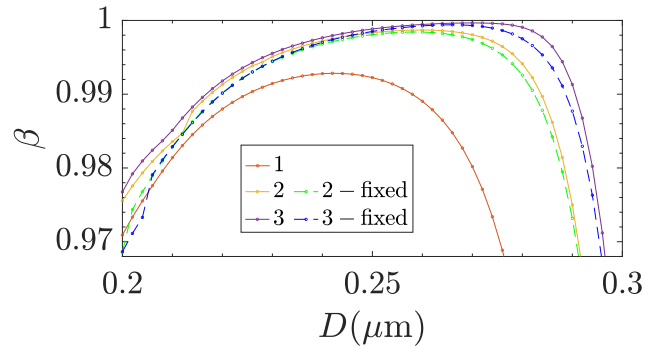


Fig. 8 Optimized β factor as a function of the wire diameter for 1 ring, 2 rings, 2 rings with fixed parameters, 3 rings, and 3 rings with fixed parameters.

In Fig. (8), the β factor is shown as a function of the wire diameter for 1 ring, 2 rings, 2 rings with fixed parameters, 3 rings, and 3 rings with fixed parameters. As seen, it is possible to increase the β factor above 0.99 in a broad diameter range and adding more rings does indeed increase the β factor further. Allowing all the parameters to be free leads to a small increase in the maximum β factor, and also slightly increases the width of the diameter range enabling very-high β values. Still, even though the radiation modes are cylindrical waves and form a continuum, the penalty of fixing the parameters for the maximum β factor is fairly small.

In Table (1), the maximum β factor, $P_{\text{HE}_{11}}/P_0$, P_R/P_0 , $P'_G/P_0 = (P_G - P_{\text{HE}_{11}})/P_0$, and the corresponding diameters and ring dimensions for the optimized rings are shown. $P_{\text{HE}_{11}}/P_0$ decreases for an increased numbers of rings due to an increased wire diameter, however, it is compensated for by the decreased emission into radiation modes to increase the β factor. Additionally, P_R/P_0 is now so small such that P'_G/P_0 , due to the higher order guided modes, is comparable in magnitude. This shows that in the absolute limit of $\beta \rightarrow 1$, the emission into higher order guided modes, introduced by the rings, is equally important as the radiation modes.

In Fig. (9), the spectra $p(k_\perp)/P_0$ for all the different numbers of rings at the optimized parameters from Table (1) are shown as a function of k_\perp/k_0 . The dotted lines correspond to the optimized

	no rings	1 ring	2 rings	2 rings - fixed	3 rings	3 rings - fixed
β_{\max}	0.9581	0.9928	0.9987	0.9984	0.9997	0.9994
$P_{\text{HE}_{11}}/P_0$	0.8845	0.8010	0.7317	0.7393	0.6945	0.7092
P_R/P_0	0.0387	0.0051	6.7e-4	7.1e-4	1.3e-4	1.8e-4
P'_G/P_0	0	6.6e-4	2.8e-4	4.5e-4	1.0e-4	2.3e-4
$D(\mu\text{m})$	0.218	0.242	0.260	0.258	0.270	0.266
$r_1(\text{nm})$		323.37	330.90	317.93	359.02	332.59
$r_2(\text{nm})$		59.03	61.58	61.66	63.97	64.03
$r_3(\text{nm})$			244.76	317.93	246.41	332.59
$r_4(\text{nm})$			67.27	61.66	71.76	64.03
$r_5(\text{nm})$					234.02	332.59
$r_6(\text{nm})$					66.92	64.03

Table 1 Maximum β factor, $P_{\text{HE}_{11}}/P_0$, P_R/P_0 , $P'_G/P_0 = (P_G - P_{\text{HE}_{11}})/P_0$, and the corresponding diameters and ring dimensions for the optimized structures.

diameters for the different numbers of rings, but without the rings themselves to directly compare the spectra. As shown, the rings in fact very efficiently suppress the emission into radiation modes for all values of k_{\perp}/k_0 .

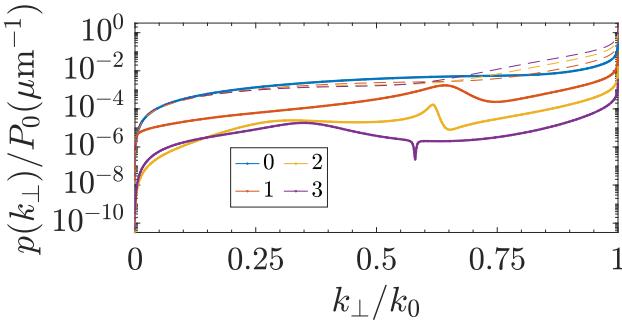


Fig. 9 The spectrum $p(k_{\perp})/P_0$ for all the different numbers of rings at the optimized parameters from Table (1) as a function of k_{\perp}/k_0 . The dotted lines correspond to the optimized diameters for the different numbers of rings but without the rings themselves for the sake of comparison.

6 Finite-size photonic nanowire

We now apply the results of the previous section, which are valid in the infinite wire approximation, to the finite sized photonic nanowire SPS^{16,25-28,79,80}. We will thus compare the photonic nanowire SPS without rings to adding one, two and three rings (only the free parameters) using the optimized parameters shown in Table 1. A sketch of the photonic nanowire SPS with rings and its geometrical parameters can be seen in Fig. (10). The central part is made of a finite-length nanowire segment, capped by a conical needle taper with half-opening angle θ and a total taper height of $h_{\text{taper}} = D/(2\tan(\theta))$. The purpose of the needle taper is to adiabatically transform the fundamental mode to increase the collection efficiency^{28,79}. At the interface between the wire and the taper, the surrounding rings, if any are added, have the same length as the nanowire segment and are terminated by a flat top surface. At the bottom there is a SiO_2 -Ag mirror⁸¹, where the SiO_2 has a thickness of t_{SiO_2} . For the refractive indices we use: $n_{\text{SiO}_2} = 1.4518$ and $n_{\text{Ag}} = 0.0747 + 6.4294i$. The QD is placed at a distance h_b (h_t) from the bottom (top) interface.

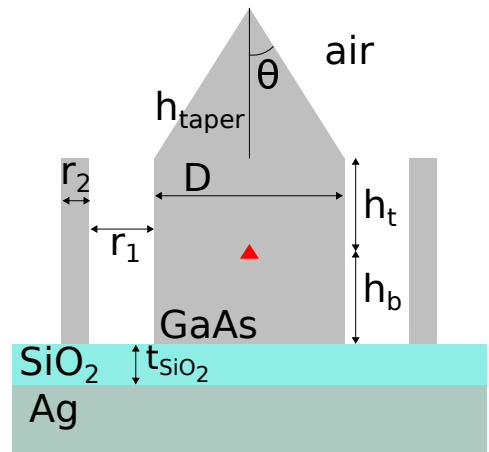


Fig. 10 Sketch of the photonic needle SPS with ring(s) and its geometrical parameters.

We will compare the full model, $\epsilon_g = P_{g,\text{lens}}/P_T$, with the single-mode model efficiency⁸⁰:

$$\epsilon_{g,\text{SMM}} = \gamma_g \frac{\beta_{\text{HE}_{11}} (1 + |r_{1,1,b}|)^2}{2(1 + \beta_{\text{HE}_{11}} |r_{1,1,b}|)}, \quad (5)$$

where $\gamma_g = P_{g,\text{HE}_{11},\text{lens}}/P_{\text{HE}_{11}}$ is the transmission coefficient of the fundamental mode. $\beta_{\text{HE}_{11}}$ is the β factor of the infinite structure and $r_{1,1,b}$ is the modal reflection of the fundamental mode at the bottom interface. In the derivation of the SMM of Eq. (5), it is assumed that the top reflection is close to 0. In supplementary (10.9), we show that the maximum reflection of the fundamental mode at the bottom interface is obtained at $t_{\text{SiO}_2} = 6\text{ nm}$ for all the different numbers of rings (including no ring). We also show how γ_g changes as a function of the tapering angle, θ , and the NA. Additionally, we show that the top reflection approaches 0 for small tapering angles, but does increase for larger tapering angles.

The vertical position of the dipole also needs to be determined and it should be placed at an antinode. For small angles of θ , the reflection of the fundamental mode at the top interface is approximately 0 and in this case there is no condition for the top height, h_t . However, when the angle increases there will be a reflection

and within the picture of a single-mode model both the top and bottom height, h_b and h_t , need to satisfy:

$$n_{b,t}2\pi = 2\beta_1 h_{b,t} + \arg(r_{1,1,b,t}), \quad n_{b,t} \in \mathbb{N}, \quad (6)$$

where β_1 is the propagation constant of the fundamental mode. n_b (n_t) thus determines the number of antinodes from the bottom (top) interface to the position of the dipole. Within the single-mode model, the choice of $n_{b,t}$ should have minimum influence on the performance of the structure, but as we will show it can indeed influence both the efficiency and the β factor (shown in supplementary (10.9)) thereby deviating from the single-mode model. As such we have tested the combined set of $n_{b,t} \in [1, 2, 3, 4]$ resulting in a total of 16 combinations.

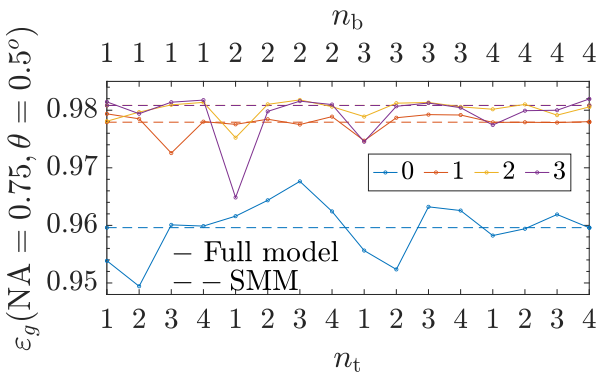


Fig. 11 Collection efficiency, $\varepsilon_g(\text{NA} = 0.75)$, as a function of the 16 different combinations of n_t and n_b for the different numbers of rings at a tapering angle of $\theta = 0.5^\circ$. The dotted line is calculated using the SMM while the solid line is the full model. The predicted values using the SMM for 2 and 3 rings is almost identical and thus the lines are overlapping.

In Fig. (11), the collection efficiency, $\varepsilon_g(\text{NA} = 0.75)$, is shown as a function of the 16 different combinations of n_t and n_b for the different numbers of rings at a tapering angle of $\theta = 0.5^\circ$. The dotted line is calculated using the SMM while the solid line is the full model. Even though the top reflection is very small there are still deviations between the full model and the SMM for all the different numbers of rings, resulting in a breakdown of the SMM. These deviation can both be positive and negative, but in general these deviations are negative except for no rings where there can be an increase of 0.0075 for $n_t = 3$ and $n_b = 2$. These deviations can be explained by the evanescent modes as there is still coupling between the fundamental mode and the evanescent modes at the interfaces, which is not quantified by the power reflections nor by the emission rates in the infinite structure. This effect decreases the further away the dipole is from interfaces as the evanescent modes decay which corresponds to larger values of n_t and n_b . However, it could indicate that in a complete optimization of the collection efficiency, the optimal heights of h_b and h_t could slightly deviate from the SMM heights. A similar effect occurs for the nanopost SPS⁸² and this effect could be quantified using the same models as in Ref.⁸². Ultimately, the maximum collection efficiencies obtained for the selected heights and $\text{NA} = 0.75$ are: $\varepsilon_{g,0} = 0.9676$, $\varepsilon_{g,1} = 0.9794$, $\varepsilon_{g,2} = 0.9818$ and $\varepsilon_{g,3} = 0.9820$ with

a total increase of 0.0143 in the maximum collection efficiency from no ring to 3 rings. The maximum collection efficiencies for the rings do not reach the values of the β factors in the infinite structures. This is because the limiting factors are now the bottom reflection and the transmission through the top taper. Nonetheless, for a multi-photon experiment with 50 photons the success probability increases by a factor of $(0.9820/0.9676)^{50} \approx 2.09$. This demonstrates that the efficiency increase, obtained by suppressing the background emission using the dielectric rings, can have a significant impact on the scale-up of photonics experiment.

For larger tapering angles, the collection efficiency is even more sensitive to the heights as is shown in supplementary (10.9).

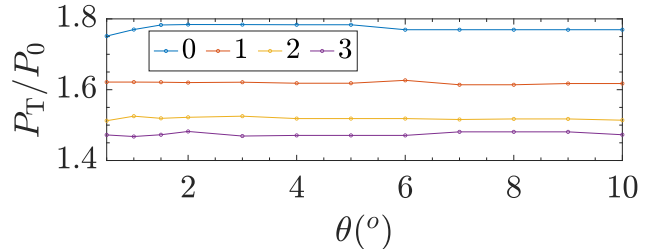


Fig. 12 Purcell factor of the total emission, P_T/P_0 , as a function of the tapering angle, θ , for the different numbers of rings where n_t and n_b are chosen such that $\varepsilon_g(\text{NA} = 0.75)$ is maximised.

The Purcell factor of the total emission, P_T/P_0 , is shown in Fig. (12) as a function of the tapering angle, θ , for the different numbers of rings where n_t and n_b are chosen such that $\varepsilon_g(\text{NA} = 0.75)$ is maximised. P_T/P_0 does not change significantly as a function of the tapering angle. As expected, P_T/P_0 depends on the numbers of rings and this is directly related to the center diameter as for the infinite structures.

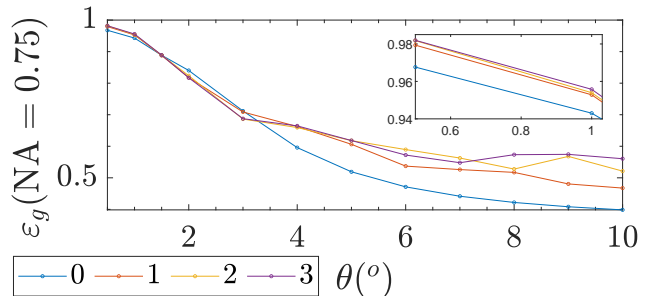


Fig. 13 Collection efficiency, $\varepsilon_g(\text{NA} = 0.75)$, as a function of the tapering angle, θ , for the different numbers of rings where n_t and n_b are chosen such that $\varepsilon_g(\text{NA} = 0.75)$ is maximised.

In Fig. (13) the collection efficiency, $\varepsilon_g(\text{NA} = 0.75)$, is shown as a function of the tapering angle, θ , for the different numbers of rings where n_t and n_b are chosen such that $\varepsilon_g(\text{NA} = 0.75)$ is maximised. The collection efficiency follows the curve for the transmission coefficient, $\gamma_g(\text{NA} = 0.75)$, shown in Fig. (20) found in supplementary (10.9), with some deviations. Generally, the collection efficiency decreases as a function of the tapering angle due to the decreased transmission coefficient. As already shown for $\theta = 0.5^\circ$, the collection efficiency can be increased for the smallest tapering angles, $\theta \leq 1.5^\circ$, using the rings. Between 2° and 3° ,

no ring performs slightly better than any of the other numbers of rings, while above 3° , no ring performs the worst.

7 Micropillar

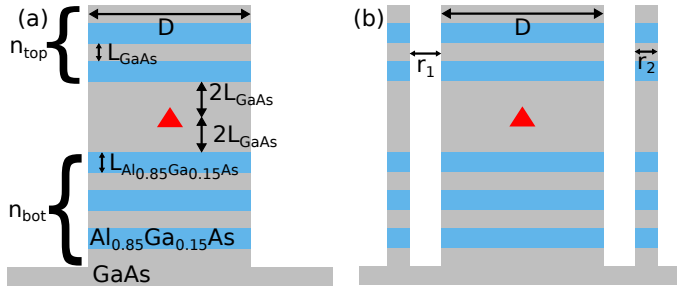


Fig. 14 (a) Sketch of the micropillar SPS and the geometrical parameters. (b) Sketch of the micropillar SPS with 1 ring. The layer thicknesses are slightly different for the micropillar with 1 ring due to the slight change in the propagation constant of the fundamental mode.

We now add rings around a micropillar SPS and show that this can improve the performance. Such a device has been investigated numerically⁸³, however, without a clear improvement in the performance. It has also been investigated for a half-micropillar SPS in the telecom O-band⁸⁴, where improvements were possible for the collection efficiency, but without reaching the performance of state-of-the-art numerically optimized SPS micropillars¹⁷. Cylindrical dielectric DBRs around the micropillar SPS have also been realized experimentally⁸⁵, where the off-resonance SE rate was decreased compared to the bulk SE rate indicating that Γ_B had been suppressed. However, the study did not include numerical simulations to analyze the improvement. Here we will consider state-of-the-art numerically optimized micropillar SPSs¹⁷ and demonstrate how the rings can further improve the performance. The optimized micropillar SPS features both large collection efficiency and indistinguishability simultaneously¹⁷. A sketch of the micropillar with and without rings and the geometrical parameters can be seen in Fig. (14). The materials are GaAs and $\text{Al}_{0.85}\text{Ga}_{0.15}\text{As}$ with $n_{\text{Al}_{0.85}\text{Ga}_{0.15}\text{As}} = 2.9982$. The DBR layer thicknesses are diameter dependent given by $L_{\text{material}} = \lambda_0 / (4n_{\text{eff,material}})$, where $n_{\text{eff,material}}$ is the effective index of the fundamental mode in the GaAs or the $\text{Al}_{0.85}\text{Ga}_{0.15}\text{As}$ obtained from the propagation constant ($\beta_1 = n_{\text{eff,material}}k_0$). The cavity thickness is $\lambda_0 / n_{\text{eff,GaAs}}$ and the dipole is placed in the center. The bottom (top) DBR contains n_{bot} (n_{top}) layer pairs. The cavity mode of the micropillar SPS is almost identical to the fundamental mode¹⁷, and we will be using β_{cav} for the β factor (Eq. (1)).

As mentioned in the introduction, the micropillar SPS utilizes the Purcell effect to increase β_{cav} and thus also features large values of F_p . Generally, F_p peaks around $D \approx 1.2 \mu\text{m}$ and then decreases for increased diameters due to an increased mode volume¹⁷. This behavior is reflected in β_{cav} which also decreases. However, more importantly to this work is the background emission Γ_B of the micropillar. For the micropillar SPS, both radiation modes and higher order guided modes contribute to Γ_B . Γ_B of the micropillar is very much diameter dependent, however, it does

not follow the peaks of the total emission rate in the infinite wire as in Fig. (5c). Instead, Γ_B features pronounced peaks exactly at the onset of the guided modes and these peaks lead to dips in β_{cav} and ε_g ⁷⁸, but with limited effect on F_p ¹⁷. These peaks thus consist on the lower diameter side of radiation modes and on the larger diameter side the newly appeared guided mode. In supplementary (10.10), we have reproduced β_{cav} , ε_g ($\text{NA} = 0.82$), P_B/P_0 , and F_p of the best performing micropillars¹⁷ with $n_{\text{bot}} = 40$ and $n_{\text{top}} = 17$ or $n_{\text{top}} = 21$. We will now choose two different diameters and add a ring. One diameter, $D = 2.2 \mu\text{m}$, corresponds to a peak in P_B/P_0 and the other diameter, $D = 2.1 \mu\text{m}$, corresponds to a local minimum in P_B/P_0 and thus a maximum in β_{cav} and ε_g ($\text{NA} = 0.82$). The micropillar with $D = 2.1 \mu\text{m}$ is therefore an optimized micropillar SPS with respect to the diameter. When the ring is added, the propagation constant of the fundamental mode, β_1 , does change very slightly, so that it should not have any influence when the first air gap is above 50 nm. Nonetheless, this has been accounted for in the following simulation. In the following we will be using $\text{NA} = 0.82$.

In Fig. (15), the (a) β_{cav} with $n_{\text{top}} = 17$, (b) β_{cav} with $n_{\text{top}} = 21$, (c) ε_g with $n_{\text{top}} = 17$, and (d) ε_g with $n_{\text{top}} = 21$ are shown as a function of the air gap, r_1 , and the ring thickness, r_2 , for 1 ring at $D = 2.2 \mu\text{m}$. The first trend observed in Fig. (15) is that regions with increased β_{cav} also show an increased ε_g , which is similar to the trend seen in the micropillar without any rings. Following the vertical axis simply corresponds to increasing the diameter and this will lead to an increase in β_{cav} and ε_g , but we are interested in whether an actual ring with an air gap can increase the performance. This is indeed possible and for some regions with $0.2 \mu\text{m} < r_1$ there is an increase both in β_{cav} and ε_g . The green dots indicate the maximum values with the restrictions of $0.2 \mu\text{m} < r_1$ and $r_2 < 0.12 \mu\text{m}$. For ε_g and $n_{\text{top}} = 17$ the following increases are obtained: from $\varepsilon_{g,17} = 0.8829$ to $\varepsilon_{g,17,1} = 0.9427$ (1 ring) with $r_1 = 0.38 \mu\text{m}$ and $r_2 = 0.08 \mu\text{m}$. For $n_{\text{top}} = 21$: from $\varepsilon_{g,21} = 0.8901$ to $\varepsilon_{g,21,1} = 0.9223$ with $r_1 = 0.36 \mu\text{m}$ and $r_2 = 0.08 \mu\text{m}$. The ring has thus efficiently suppressed the background emission into radiation modes and close-to-cutoff guided modes, which are at the origin of the performance decrease for a $D = 2.2 \mu\text{m}$ micropillar. Therefore the ring improves the performance of this micropillar to values that are very close to the ones of a micropillar with an optimal diameter.

In Fig. (16), we now present the same scan of the ring parameters as in Fig. (15) but now for $D = 2.1 \mu\text{m}$. Again, regions with an increased β_{cav} generally overlap with an increased ε_g , however, with some deviations for $n_{\text{top}} = 21$. Ultimately, the collection efficiency can be increased from $\varepsilon_{g,17} = 0.9497$ to $\varepsilon_{g,17,1} = 0.9582$ at $r_1 = 0.72 \mu\text{m}$ and $r_2 = 0.06 \mu\text{m}$ and for $n_{\text{top}} = 21$ from $\varepsilon_{g,21} = 0.9529$ to $\varepsilon_{g,21,1} = 0.9571$ at $r_1 = 0.24 \mu\text{m}$ and $r_2 = 0.12 \mu\text{m}$. As such the ring can still slightly improve the performance of the micropillar with an optimal diameter. However, a major part of the background emission is into higher order guided modes and the ring offers no suppression mechanism of these modes and therefore P_B/P_0 is not reduced to the same level as for the small diameter range of the infinite wire.

In supplementary (10.10), we also show β_{cav} and ε_g for 2 rings with fixed parameters surrounding the micropillar with

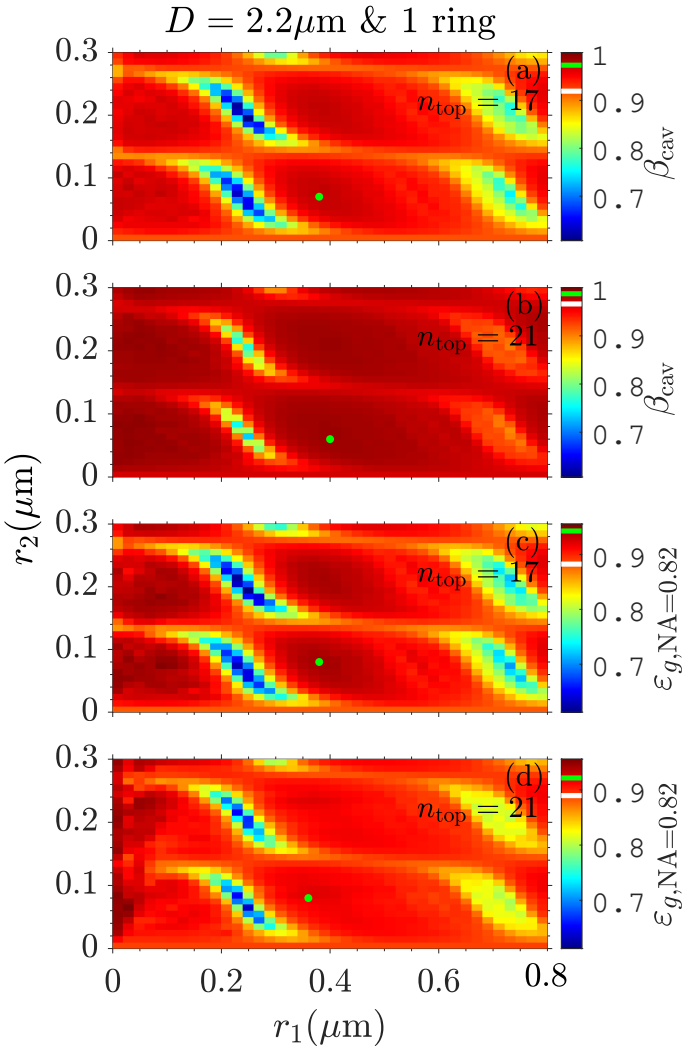


Fig. 15 (a) β_{cav} with $n_{\text{top}} = 17$, (b) β_{cav} with $n_{\text{top}} = 21$, (c) $\epsilon_g(\text{NA} = 0.82)$ with $n_{\text{top}} = 17$, and (d) $\epsilon_g(\text{NA} = 0.82)$ with $n_{\text{top}} = 21$ as a function of the air gap, r_1 , and the ring thickness, r_2 , for 1 ring at $D = 2.2 \mu\text{m}$. The green dots indicate the maximum values with the restrictions of $0.2 \mu\text{m} < r_1$ and $r_2 < 0.12 \mu\text{m}$. The white line in the colorbars indicates the value without a ring and the green line indicates the value at the green dot.

$D = 2.1 \mu\text{m}$. Here the collection efficiency reaches a maximum of $\epsilon_{g,17,2} = 0.9610$ at $r_1 = 0.13 \mu\text{m}$ and $r_2 = 0.08 \mu\text{m}$. Thus, with the test of 1 to 2 rings around the micropillar showing a potential increase in the collection efficiency of 0.008 from $\epsilon_{g,21} = 0.9529$ with no rings to $\epsilon_{g,17,2} = 0.9610$ with 2 rings, corresponding to a reduction in the losses from 4.7% to 3.9%, we have shown that the rings can indeed further push the boundary of the optimized micropillar.

8 Discussion

We have shown that a few rings around the infinite wire can increase the β factor up to 0.99 in the small diameter regime of $D = 220 \text{ nm}$ to $D = 290 \text{ nm}$ by suppressing the emission into radiation modes. For two and three rings it was even possible to achieve a β factor up to 0.999. We then applied this result to the photonic nanowire SPS, which led to an increase in the maximum collection efficiency obtained at the smallest tapering

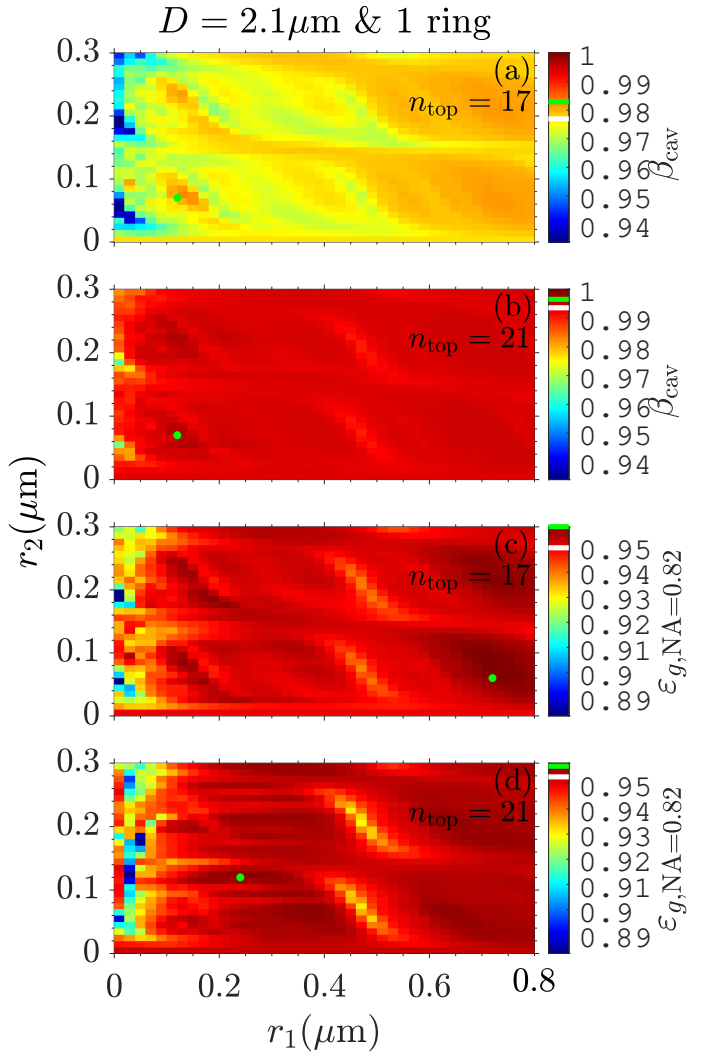


Fig. 16 (a) β_{cav} with $n_{\text{top}} = 17$, (b) β_{cav} with $n_{\text{top}} = 21$, (c) $\epsilon_g(\text{NA} = 0.82)$ with $n_{\text{top}} = 17$, and (d) $\epsilon_g(\text{NA} = 0.82)$ with $n_{\text{top}} = 21$ as a function of the air gap, r_1 , and the ring thickness, r_2 , for 1 ring at $D = 2.1 \mu\text{m}$. The green dots indicate the maximum values without any restrictions. The white line in the colorbars indicates the value without a ring and the green line indicates the value at the green dot. Note: a few of the darkest blue data points have lower values than indicated by the color bars, but the limit is chosen to increase the visibility.

angles, $\theta \leq 1.5^\circ$. The reason for why we could directly apply the result of the infinite wire is that the physics of the photonic nanowire is generally viewed as single-moded⁸⁰. There is only one guided mode, the fundamental mode, due to the small diameter and the fundamental mode does not scatter significantly into radiation modes at the optimized bottom mirror, nor any back-scattering at the top needle taper with a small tapering angle. However, we also varied the position of the dipole by placing it at different antinodes and here we observed fairly significant deviations from the SMM. This could be explained by the coupling to and from the evanescent modes and as such leaves room for further optimization of the height of the straight nanowire section and the position of the dipole. Still, the limiting factors to increase the collection efficiency towards unity for the photonic nanowire SPS are the transmission coefficient and the bottom re-

flection. One extra detail is that for each added ring, the diameter of the central nanowire for the maximum value of the β factor slightly increased. This leads to slightly longer structures for the needle tapering, but this would instead be an advantage for trumpet tapers^{16,28,80,86,87}.

For larger diameters, it was also possible to increase the β factor of the infinite wire. However, the absolute increase was not as large as for the smaller diameters, because it is the higher-order guided modes which constitute the main contribution to the background emission, for which the rings do not offer any control. Still, we wanted to put rings around the micropillar SPS which typically features diameters in the 2-4 μm range. However, the background emission, Γ_B , of the micropillar follows a different pattern than the background emission of the infinite wire and therefore we could not directly apply the optimized ring parameters of the infinite wire to the micropillar. Nonetheless, at a suboptimal diameter where Γ_B peaks, the ring could suppress Γ_B close to a level of an optimal diameter such that the collection efficiency significantly increased. At an optimal diameter, 1-2 rings could still slightly increase the collection efficiency. However, we observe in Fig. (16) slightly different behaviours between the β factor and the collection efficiency. This shows that a SMM is not sufficient to capture fully the effects of the rings. The demanding complete optimization of micropillars with rings, using the full modal model presented in this paper, goes beyond the scope of the present paper and is left for future work.

9 Conclusions

We have provided a detailed physical description of how cylindrical rings around an infinite wire influence the emission rates into the guided modes and the radiation modes. This was done by making use of a fully analytical method, allowing for in-depth analysis and fast computations. We then demonstrated that a few rings could further suppress the emission into radiation modes, such that we could achieve β factors up to 0.999. This result was then applied to the photonic nanowire SPS, which led to an increase in the maximum collection efficiency from $\epsilon_{g,0} = 0.9676$ without any rings to $\epsilon_{g,3} = 0.9820$ with three rings; further pushing the theoretical limit toward near-unity collection efficiency. This increase in the collection efficiency corresponds to an increase in the success probability of a multi-photon interference experiment with 50 photons by a factor of $(0.9820/0.9676)^{50} \approx 2.09$. We also simulated rings around the micropillar SPS for which it was also possible to further increase the collection efficiency from $\epsilon_g = 0.9529$ to $\epsilon_g = 0.9610$.

Author Contributions

N.G. formulated the project. M.A.J. developed the analytical method and performed the simulations. M.A.J. wrote the manuscript with comments from all authors. N.G. and L.V. supervised the project.

Conflicts of interest

There are no conflicts to declare.

Acknowledgements

This work is funded by the European Research Council (ERC-CoG “UNITY,” Grant No. 865230), the French National Research Agency (Grant No. ANR-19-CE47-0009-02), the European Union’s Horizon 2020 Research and Innovation Programme under the Marie Skłodowska-Curie Grant (Agreement No. 861097), and by the Independent Research Fund Denmark (Grant No. DFF-9041-00046B).

References

- Y. Arakawa and M. J. Holmes, *Appl. Phys. Rev.*, 2020, **7**, 021309.
- I. Aharonovich, D. Englund and M. Toth, *Nat. Photonics*, 2016, **10**, 631–641.
- N. GregerSEN, P. Kaer and J. Mørk, *IEEE J. Sel. Top. Quantum Electron.*, 2013, **19**, 9000516.
- N. GregerSEN, D. P. S. McCutcheon and J. Mørk, *Handbook of Optoelectronic Device Modeling and Simulation* Vol. 2, CRC Press, Boca Raton, 2017, ch. 46, pp. 585–607.
- D. Huber, M. Reindl, J. Aberl, A. Rastelli and R. Trotta, *J. Opt.*, 2018, **20**, 073002.
- J.-W. Pan, Z.-B. Chen, C.-Y. Lu, H. Weinfurter, A. Zeilinger and M. Zukowski, *Rev. Mod. Phys.*, 2012, **84**, 777–838.
- J. L. O’Brien, A. Furusawa and J. Vučković, *Nat. Photonics*, 2009, **3**, 687–695.
- J.-M. Gérard and B. Gayral, *Journal of Lightwave Technology*, 1999, **17**, 2089–2095.
- P. Michler, A. Kiraz, C. Becher, W. V. Schoenfeld, P. M. Petroff, L. Zhang, E. Hu and A. Imamoglu, *Science*, 2000, **290**, 2282–2285.
- C. Santori, D. Fattal, J. Vučković, G. S. Solomon and Y. Yamamoto, *Nature*, 2002, **419**, 594–597.
- A. J. Shields, *Nat. Photonics*, 2007, **1**, 215–223.
- W. L. Barnes, G. Björk, J. M. Gérard, P. Jonsson, J. A. E. Wasey, P. T. Worthing and V. Zwillaer, *The European Physical Journal D - Atomic, Molecular, Optical and Plasma Physics*, 2002, **18**, 197–210.
- J. M. Gérard, B. Sermage, B. Gayral, B. Legrand, E. Costard and V. Thierry-Mieg, *Phys. Rev. Lett.*, 1998, **81**, 1110–1113.
- E. M. Purcell, *Phys. Rev.*, 1946, **69**, 681.
- I. Friedler, C. Sauvan, J. P. Hugonin, P. Lalanne, J. Claudon and J. M. Gérard, *Opt. Express*, 2009, **17**, 2095–2110.
- N. GregerSEN, D. P. S. McCutcheon, J. Mørk, J.-M. Gérard and J. Claudon, *Opt. Express*, 2016, **24**, 20904–20924.
- B.-Y. Wang, E. V. Denning, U. M. Gür, C.-Y. Lu and N. GregerSEN, *Phys. Rev. B*, 2020, **102**, 125301.
- N. Somaschi, V. Giesz, L. De Santis, J. C. Loredo, M. P. Almeida, G. Hornecker, S. L. Portalupi, T. Grange, C. Antón, J. Demory, C. Gómez, I. Sagnes, N. D. Lanzillotti-Kimura, A. Lemaître, A. Auffeves, A. G. White, L. Lanco and P. Senellart, *Nat. Photonics*, 2016, **10**, 340–345.
- E. Moreau, I. Robert, J. M. Gérard, I. Abram, L. Manin and V. Thierry-Mieg, *Applied Physics Letters*, 2001, **79**, 2865–2867.

20 H. Wang, Y.-M. He, T.-H. Chung, H. Hu, Y. Yu, S. Chen, X. Ding, M.-C. Chen, J. Qin, X. Yang, R.-Z. Liu, Z.-C. Duan, J.-P. Li, S. Gerhardt, K. Winkler, J. Jurkat, L.-J. Wang, N. Gregersen, Y.-H. Huo, Q. Dai, S. Yu, S. Höfling, C.-Y. Lu and J.-W. Pan, *Nat. Photonics*, 2019, **13**, 770–775.

21 X. Ding, Y. He, Z.-C. Duan, N. Gregersen, M.-C. Chen, S. Unsleber, S. Maier, C. Schneider, M. Kamp, S. Höfling, C.-Y. Lu and J.-W. Pan, *Phys. Rev. Lett.*, 2016, **116**, 020401.

22 N. Tomm, A. Javadi, N. O. Antoniadis, D. Najer, M. C. Löbl, A. R. Korsch, R. Schott, S. R. Valentin, A. D. Wieck, A. Ludwig and R. J. Warburton, *Nat. Nanotechnol.*, 2021, **16**, 399–403.

23 J. Iles-Smith, D. P. S. McCutcheon, A. Nazir and J. Mørk, *Nature Photonics*, 2017, **11**, 521–526.

24 B. Gaál, L. Vannucci, M. A. Jacobsen, J. Claudon, J.-M. Gérard and N. Gregersen, *Applied Physics Letters*, 2022, **121**, 170501.

25 J. Bleuse, J. Claudon, M. Creasey, N. S. Malik, J.-M. Gérard, I. Maksymov, J.-P. Hugonin and P. Lalanne, *Phys. Rev. Lett.*, 2011, **106**, 103601.

26 J. Claudon, J. Bleuse, N. S. Malik, M. Bazin, P. Jaffrennou, N. Gregersen, C. Sauvan, P. Lalanne and J.-M. Gérard, *Nat. Photonics*, 2010, **4**, 174–177.

27 J. Claudon, N. Gregersen, P. Lalanne and J.-M. Gérard, *ChemPhysChem*, 2013, **14**, 2393–2402.

28 M. Munsch, N. S. Malik, E. Dupuy, A. Delga, J. Bleuse, J.-M. Gérard, J. Claudon, N. Gregersen and J. Mørk, *Phys. Rev. Lett.*, 2013, **110**, 177402.

29 G. Lecamp, P. Lalanne and J. P. Hugonin, *Phys. Rev. Lett.*, 2007, **99**, 023902.

30 V. S. C. Manga Rao and S. Hughes, *Phys. Rev. B*, 2007, **75**, 205437.

31 M. Arcari, I. Söllner, A. Javadi, S. Lindskov Hansen, S. Mahmoodian, J. Liu, H. Thyrrstrup, E. H. Lee, J. D. Song, S. Stobbe and P. Lodahl, *Phys. Rev. Lett.*, 2014, **113**, 093603.

32 X. Zhou, P. Lodahl and L. Midolo, *Quantum Science and Technology*, 2022, **7**, 025023.

33 B. Da Lio, C. Faurby, X. Zhou, M. L. Chan, R. Uppu, H. Thyrrstrup, S. Scholz, A. D. Wieck, A. Ludwig, P. Lodahl and L. Midolo, *Advanced Quantum Technologies*, 2022, **5**, 2200006.

34 F. T. Østfeldt, E. M. González-Ruiz, N. Hauff, Y. Wang, A. D. Wieck, A. Ludwig, R. Schott, L. Midolo, A. S. Sørensen, R. Uppu and P. Lodahl, *PRX Quantum*, 2022, **3**, 020363.

35 M. Davanço, M. T. Rakher, D. Schuh, A. Badolato and K. Srinivasan, *Applied Physics Letters*, 2011, **99**, 041102.

36 S. Ates, L. Sapienza, M. Davanco, A. Badolato and K. Srinivasan, *IEEE Journal of Selected Topics in Quantum Electronics*, 2012, **18**, 1711–1721.

37 B. Yao, R. Su, Y. Wei, Z. Liu, T. Zhao and J. Liu, *J. Korean Phys. Soc.*, 2018, **73**, 1502–1505.

38 J. Liu, R. Su, Y. Wei, B. Yao, S. F. C. da Silva, Y. Yu, J. Iles-Smith, K. Srinivasan, A. Rastelli, J. Li and X. Wang, *Nat. Nanotechnol.*, 2019, **14**, 586–593.

39 H. Wang, H. Hu, T.-H. Chung, J. Qin, X. Yang, J.-P. Li, R.-Z. Liu, H.-S. Zhong, Y.-M. He, X. Ding, Y.-H. Deng, Q. Dai, Y.-H. Huo, S. Höfling, C.-Y. Lu and J.-W. Pan, *Phys. Rev. Lett.*, 2019, **122**, 113602.

40 L. Rickert, T. Kupko, S. Rodt, S. Reitzenstein and T. Heindel, *Opt. Express*, 2019, **27**, 36824–36837.

41 M. Moczała-Dusanowska, L. Dusanowski, O. Iff, T. Huber, S. Kuhn, T. Czyszanowski, C. Schneider and S. Höfling, *ACS Photonics*, 2020, **7**, 3474–3480.

42 Y. Jiang and J. Hacker, *Applied Physics Letters*, 1993, **63**, 1453–1455.

43 Y. Jiang and J. Hacker, *Appl. Opt.*, 1994, **33**, 7431–7434.

44 Y. Jiang and J. Hacker, *Cylindrical-wave controlling, generating and guiding devices*, 1994, US Patent 5,357,591.

45 V. V. Nikolaev, G. S. Sokolovskii and M. A. Kaliteevskii, *Semiconductors*, 1999, **33**, 147–152.

46 M. A. Kaliteevski, R. A. Abram, V. V. Nikolaev and G. S. Sokolovskii, *Journal of Modern Optics*, 1999, **46**, 875–890.

47 M. A. Kaliteevski, R. A. Abram and V. V. Nikolaev, *Journal of Modern Optics*, 2000, **47**, 677–684.

48 M. A. Kaliteevskii and V. V. Nikolaev, *Technical Physics*, 2000, **45**, 865–869.

49 D. Ochoa, R. Houdré, M. Ilegems, H. Benisty, T. F. Krauss and C. J. M. Smith, *Phys. Rev. B*, 2000, **61**, 4806–4812.

50 J. Scheuer and A. Yariv, *Opt. Express*, 2003, **11**, 2736–2746.

51 J. Scheuer and A. Yariv, *J. Opt. Soc. Am. B*, 2003, **20**, 2285–2291.

52 L. Novotny and B. Hecht, *Principles of Nano-Optics*, Cambridge University Press, 2012.

53 D. P. Nyquist, D. R. Johnson and S. V. Hsu, *J. Opt. Soc. Am.*, 1981, **71**, 49–54.

54 A. Lavrinenko, J. Lægsgaard, N. Gregersen, F. Schmidt and T. Søndergaard, *Numerical Methods in Photonics*, CRC Press, 2014.

55 P. Yeh, A. Yariv and E. Marom, *J. Opt. Soc. Am.*, 1978, **68**, 1196–1201.

56 A. B. Manenkov, *Radiophysics and Quantum Electronics*, 1970, **13**, 578–586.

57 A. W. Snyder, *IEEE Transactions on Microwave Theory and Techniques*, 1971, **19**, 720–727.

58 R. A. Sammut, *PhD thesis*, The Australian National University, 1975.

59 C. Vassallo, *J. Opt. Soc. Am.*, 1981, **71**, 1282–1282.

60 V. V. Shevchenko, *Radio Science*, 1982, **17**, 229–231.

61 R. A. Sammut, *J. Opt. Soc. Am.*, 1982, **72**, 1335–1337.

62 C. Vassallo, *J. Opt. Soc. Am.*, 1983, **73**, 680–683.

63 A. W. Snyder and J. D. Love, *Optical waveguide theory*, Springer New York, NY, 1983.

64 I. Tigelis, C. N. Capsalis and N. K. Uzunoglu, *International Journal of Infrared and Millimeter Waves*, 1987, **8**, 1053–1068.

65 N. Morita, *Journal of Electromagnetic Waves and Applications*, 1988, **2**, 445–457.

66 L. Alvarez and M. Xiao, *Journal of Electromagnetic Waves and*

Applications, 2005, **19**, 933–951.

67 J. Scheuer, W. M. J. Green, G. DeRose and A. Yariv, *Opt. Lett.*, 2004, **29**, 2641–2643.

68 J. Scheuer, W. M. J. Green, G. A. DeRose and A. Yariv, *Applied Physics Letters*, 2005, **86**, 251101.

69 J. Scheuer, W. Green, G. DeRose and A. Yariv, *IEEE Journal of Selected Topics in Quantum Electronics*, 2005, **11**, 476–484.

70 J. Scheuer, *J. Opt. Soc. Am. B*, 2007, **24**, 2178–2184.

71 A. Jebali, D. Erni, S. Gulde, R. F. Mahrt and W. Bächtold, *J. Opt. Soc. Am. B*, 2007, **24**, 906–915.

72 O. Weiss and J. Scheuer, *Applied Physics Letters*, 2010, **97**, 251108.

73 N. Doran and K. Blow, *Journal of Lightwave Technology*, 1983, **1**, 588–590.

74 S. G. Johnson, M. Ibanescu, M. Skorobogatiy, O. Weisberg, T. D. Engeness, M. Soljačić, S. A. Jacobs, J. D. Joannopoulos and Y. Fink, *Opt. Express*, 2001, **9**, 748–779.

75 N. Doran and K. Blow, *Journal of Lightwave Technology*, 1983, **1**, 588–590.

76 G. Vienne, Y. Xu, C. Jakobsen, H. Deyerl, T. Hansen, B. Larsen, J. Jensen, T. Sorensen, M. Terrel, Y. Huang, R. Lee, N. Mortensen, J. Broeng, H. Simonsen, A. Bjarklev and A. Yariv, Optical Fiber Communication Conference, 2004. OFC 2004, 2004, pp. 3 pp. vol.2–.

77 J. Scheuer, W. M. J. Green, G. DeRose and A. Yariv, 2004, **5333**, 183 – 194.

78 B.-Y. Wang, T. Häyrynen, L. Vannucci, M. A. Jacobsen, C.-Y. Lu and N. Gregersen, *Applied Physics Letters*, 2021, **118**, 114003.

79 N. Gregersen, T. R. Nielsen, J. Claudon, J.-M. Gérard and J. Mørk, *Opt. Lett.*, 2008, **33**, 1693–1695.

80 N. Gregersen, T. R. Nielsen, J. Mørk, J. Claudon and J.-M. Gérard, *Opt. Express*, 2010, **18**, 21204–21218.

81 I. Friedler, P. Lalanne, J. P. Hugonin, J. Claudon, J. M. Gérard, A. Beveratos and I. Robert-Philip, *Opt. Lett.*, 2008, **33**, 2635–2637.

82 M. A. Jacobsen, Y. Wang, L. Vannucci, J. Claudon, J.-M. Gérard and N. Gregersen, *Nanoscale*, 2023, **15**, 6156–6169.

83 Y.-L. D. Ho, T. Cao, P. S. Ivanov, M. J. Cryan, I. J. Craddock, C. J. Railton and J. G. Rarity, *IEEE Journal of Quantum Electronics*, 2007, **43**, 462–472.

84 S. A. Blokhin, M. A. Bobrov, N. A. Maleev, J. N. Donges, L. Bremer, A. A. Blokhin, A. P. Vasil'ev, A. G. Kuzmenkov, E. S. Kolodeznyi, V. A. Shchukin, N. N. Ledentsov, S. Reitzenstein and V. M. Ustinov, *Opt. Express*, 2021, **29**, 6582–6598.

85 T. Jakubczyk, H. Franke, T. Smoleński, M. Ściesiek, W. Pacuski, A. Golnik, R. Schmidt-Grund, M. Grundmann, C. Kruse, D. Hommel and P. Kossacki, *ACS Nano*, 2014, **8**, 9970–9978.

86 P. Stepanov, A. Delga, N. Gregersen, E. Peinke, M. Munsch, J. Teissier, J. Mørk, M. Richard, J. Bleuse, J.-M. Gérard and J. Claudon, *Applied Physics Letters*, 2015, **107**, 141106.

87 D. Cadeddu, J. Teissier, F. R. Braakman, N. Gregersen, P. Stepanov, J.-M. Gérard, J. Claudon, R. J. Warburton, M. Poggio and M. Munsch, *Applied Physics Letters*, 2016, **108**, 011112.

88 U. M. Gür, S. Arslanagić, M. Mattes and N. Gregersen, *Phys. Rev. E*, 2021, **103**, 033301.

89 T. Häyrynen, J. R. de Lasson and N. Gregersen, *Journal of the Optical Society of America A*, 2016, **33**, 1298.

90 C. A. Balanis, *Advanced Engineering Electromagnetics*, Wiley, New York, 1st edn, 1989.

91 A. Yariv and P. Yeh, *Photonics: Optical Electronics in Modern Communications*, Oxford University Press, 6th edn, 2007.

92 C. Yeh and G. Lindgren, *Appl. Opt.*, 1977, **16**, 483–493.

93 K. Morishita, Y. Obata and N. Kumagai, *IEEE Transactions on Microwave Theory and Techniques*, 1982, **30**, 1821–1826.

94 M. A. Kaliteevskii, V. V. Nikolaev and R. A. Abram, *Optics and Spectroscopy*, 2000, **88**, 792–795.

95 D. Y. K. Ko and J. R. Sambles, *J. Opt. Soc. Am. A*, 1988, **5**, 1863–1866.

96 S. García and I. Gasulla, *IEEE Journal of Selected Topics in Quantum Electronics*, 2020, **26**, 1–11.

97 X. Xie and Y. Zhang, *Journal of Lightwave Technology*, 2022, **40**, 785–796.

98 T. M. Inc., *MATLAB version: 9.11.0 (R2021b)*, 2021, <https://www.mathworks.com>.

99 U. Langbein, U. Trutschel, A. Unger and M. Duguay, *Optical and Quantum Electronics*, 2009, **41**, 223–233.

100 W. C. Chew, *GEOPHYSICS*, 1984, **49**, 81–91.

101 J. R. Lovell and W. C. Chew, *IEEE Transactions on Geoscience and Remote Sensing*, 1987, **GE-25**, 850–858.

102 W. C. Chew, *Waves and Fields in Inhomogenous Media*, Wiley-IEEE Press, 1995.

103 D. Bhattacharya, B. Ghosh, M. Sinha and A. A. Kishk, *IET Microwaves, Antennas & Propagation*, 2020, **14**, 1027–1037.

104 D. Hong, *IEEE Transactions on Geoscience and Remote Sensing*, 2022, **60**, 1–16.

105 G. B. Arfken and H. J. Weber, *Mathematical Methods for Physicists (sixth Edition)*, Elsevier Academic Press, Boston, sixth Edition edn, 2005, pp. 675–739.

106 N. K. Uzunoglu, C. N. Capsalis and I. Tigelis, *J. Opt. Soc. Am. A*, 1987, **4**, 2150–2157.

107 T. M. Inc., *fmincon*, 2023, <https://se.mathworks.com/help/optim/ug/fmincon.html>.

108 T. M. Inc., *fminsearch*, 2023, <https://se.mathworks.com/help/matlab/ref/fminsearch.html>.

109 J. D'Errico, *fminsearchbnd,fminsearchcon*, 2023, <https://www.mathworks.com/matlabcentral/fileexchange/8277-fminsearchbnd,fminsearchcon>.

110 T. M. Inc., *patternsearch*, 2023, <https://se.mathworks.com/help/gads/patternsearch.html>.

10 Supplementary

10.1 Numerical methods

For the structures which extend infinitely the eigenmodes will be found analytically, whereas for the finite sized structures the eigenmodes will be found using the FMM with open boundary conditions⁸⁸ and a non-equidistant discretization scheme^{88,89} which can easily be combined with a standard scattering matrix formalism⁵⁴ to calculate the electromagnetic field and the normalized emission rates. A near- to far-field transformation is then utilized⁹⁰ along with a Gaussian field overlap (see appendix of Ref.¹⁷) to calculate the collection efficiency.

We will now provide a bit more information on how the eigenmodes can be found analytically. There are several studies and articles of the radiation modes of a dielectric wire or more generally a waveguide with open boundary conditions^{53,56–66}. Here we will also consider structures with more layers in the radial direction compared to the nanowire, but still the orthogonalization condition/procedure is exactly the same and the transfer matrix formalism for cylindrical structures⁵⁵ can easily be applied to obtain the continuum of radiation modes for arbitrary radial index profiles with cylindrical symmetry. To the best of our knowledge, the radiation modes for such a structure have not been explicitly constructed before. The mathematical formulation will be outlined in the following sections.

Descriptions of the guided modes of the wire are text-book material⁹¹, while for cylindrical structures with additional layers there are several different analytical methods to describe the guided modes. Variations of the transfer matrix formalism^{92–94} can be used to obtain the guided modes, however this method becomes numerically unstable for larger radii and more rings due to the exponentially decreasing and increasing modified Bessel functions of $K_m(k_\perp r)$ and $I_m(k_\perp r)$ in the low refractive index regions. This is a classic challenge of the transfer matrix method in general^{54,95}, which does not occur for the radiation modes as they only include the Bessel functions of $J_m(k_\perp r)$ and $Y_m(k_\perp r)$. Another method is to build a larger matrix^{96,97}, where the size of the matrix depends on the number of radial layers. The advantage of this method is that all the elements can be scaled and thus avoid the simultaneously exponentially decreasing and increasing terms making the method much more numerically stable. The disadvantage is that one has to calculate the determinant of an ever increasing matrix, however in^{96,97} algorithms are provided to ease the calculation, though we generally found it sufficient to simply let MATLAB⁹⁸ evaluate the determinant. This is the method, which has been used in this paper and it is outlined in the following sections. Another alternative also exists⁹⁹ to determine the guided modes of the multi-layered cylindrical structure.

Alternatively, the scattering matrix formalism of cylindrical structures developed by Chew^{100–104} could solve the problem of a dipole in the multi-layered cylindrical structure.

10.2 Radiation modes of infinite wire

We are solving Maxwell's equations in the frequency domain in a cylindrical coordinate system. We have applied the following scaling of the magnetic field: $\mathbf{H}' = \omega\mu_0\mathbf{H}$. As the refractive index is constant in the z-direction the fields can be written as: $\mathbf{E}(\mathbf{r}) = \mathbf{E}(\mathbf{r}_\perp)e^{i\beta z}$ and $\mathbf{H}(\mathbf{r}) = \mathbf{H}(\mathbf{r}_\perp)e^{i\beta z}$ for forward propagation. The in-plane components of the electromagnetic field can then be related to the z-components, derived from Maxwell's equations, using the following expressions⁸⁸:

$$\begin{aligned}
E_r(r, \phi) &= i \frac{1}{k_\perp^2} \frac{\partial_\phi H_z(r, \phi)}{r} + i \frac{\beta}{k_\perp^2} \partial_r E_z(r, \phi) \\
E_\phi(r, \phi) &= i \frac{\beta}{k_\perp^2} \frac{\partial_\phi E_z(r, \phi)}{r} - i \frac{1}{k_\perp^2} \partial_r H_z(r, \phi) \\
H_r(r, \phi) &= -i \frac{k_0^2 n^2}{k_\perp^2} \frac{\partial_\phi E_z(r, \phi)}{r} + i \frac{\beta}{k_\perp^2} \partial_r H_z(r, \phi) \\
H_\phi(r, \phi) &= i \frac{\beta}{k_\perp^2} \frac{\partial_\phi H_z(r, \phi)}{r} + i \frac{k_0^2 n^2}{k_\perp^2} \partial_r E_z(r, \phi),
\end{aligned} \tag{7}$$

where $k_0 = 2\pi/\lambda_0$ is the free-space wavenumber (λ_0 is the free-space wavelength), n is the refractive index, and $k_\perp = \sqrt{n^2 k_0^2 - \beta^2}$ is the in-plane k -value. Eq. (7) is locally valid in every region with constant refractive index. For the wire we have two regions, namely the wire (1) and the surrounding air (2). The z-components are the solutions to the Helmholtz equation and in the wire region we obtain:

$$\begin{aligned}
E_{1,z}(r, \phi) &= -iA_1 J_m(k_{1,\perp} r) \cos(m\phi) \\
H_{1,z}(r, \phi) &= -iB_1 J_m(k_{1,\perp} r) \sin(m\phi)
\end{aligned} \tag{8}$$

One could also have chosen $\sin(m\phi)$ for E_z and $\cos(m\phi)$ for H_z , which would result in orthogonal polarization. However, with the choice in Eq. (8), the polarization matches a dipole oriented along the x-axis ($\phi = 0$). The $-i$ is a convenient choice for the normalization later. In the air region we obtain the following solution:

$$\begin{aligned}
E_{2,z}(r, \phi) &= -i(A_2 J_m(k_{2,\perp} r) + C_2 Y_m(k_{2,\perp} r)) \cos(m\phi) \\
H_{2,z}(r, \phi) &= -i(B_2 J_m(k_{2,\perp} r) + D_2 J_m(k_{2,\perp} r)) \sin(m\phi)
\end{aligned} \tag{9}$$

Inserting Eq. (8) into Eq. (7) the following expressions are obtained for the wire region:

$$\begin{aligned}
E_{1,r}(r, \phi) &= \frac{\beta}{k_{1,\perp}^2} \left(B_1 \frac{m J_m(k_{1,\perp} r)}{\beta} + A_1 \partial_r J_m(k_{1,\perp} r) \right) \cos(m\phi) \\
E_{1,\phi}(r, \phi) &= -\frac{\beta}{k_{1,\perp}^2} \left(A_1 m \frac{J_m(k_{1,\perp} r)}{r} + B_1 \frac{1}{\beta} \partial_r J_m(k_{1,\perp} r) \right) \sin(m\phi) \\
H_{1,r}(r, \phi) &= \frac{\beta}{k_{1,\perp}^2} \left(A_1 m \frac{k_0^2 n_1^2}{\beta} \frac{J_m(k_{1,\perp} r)}{r} + B_1 \partial_r J_m(k_{1,\perp} r) \right) \sin(m\phi) \\
H_{1,\phi}(r, \phi) &= \frac{\beta}{k_{1,\perp}^2} \left(B_1 m \frac{J_m(k_{1,\perp} r)}{r} + A_1 \frac{k_0^2 n_1^2}{\beta} \partial_r J_m(k_{1,\perp} r) \right) \cos(m\phi)
\end{aligned} \tag{10}$$

and for the air region:

$$\begin{aligned}
E_{2,r}(r, \phi) &= \frac{\beta}{k_{2,\perp}^2} \left(B_2 \frac{m J_m(k_{2,\perp} r)}{\beta} + A_2 \partial_r J_m(k_{2,\perp} r) + D_2 \frac{m Y_m(k_{2,\perp} r)}{\beta} + C_2 \partial_r Y_m(k_{2,\perp} r) \right) \cos(m\phi) \\
E_{2,\phi}(r, \phi) &= -\frac{\beta}{k_{2,\perp}^2} \left(A_2 m \frac{J_m(k_{2,\perp} r)}{r} + B_2 \frac{1}{\beta} \partial_r J_m(k_{2,\perp} r) + C_2 m \frac{Y_m(k_{2,\perp} r)}{r} + D_2 \frac{1}{\beta} \partial_r Y_m(k_{2,\perp} r) \right) \sin(m\phi) \\
H_{2,r}(r, \phi) &= \frac{\beta}{k_{2,\perp}^2} \left(A_2 m \frac{k_0^2 n_2^2}{\beta} \frac{J_m(k_{2,\perp} r)}{r} + B_2 \partial_r J_m(k_{2,\perp} r) + C_2 m \frac{k_0^2 n_2^2}{\beta} \frac{Y_m(k_{2,\perp} r)}{r} + D_2 \partial_r Y_m(k_{2,\perp} r) \right) \sin(m\phi) \\
H_{2,\phi}(r, \phi) &= \frac{\beta}{k_{2,\perp}^2} \left(B_2 m \frac{J_m(k_{2,\perp} r)}{r} + A_2 \frac{k_0^2 n_2^2}{\beta} \partial_r J_m(k_{2,\perp} r) + D_2 m \frac{Y_m(k_{2,\perp} r)}{r} + C_2 \frac{k_0^2 n_2^2}{\beta} \partial_r Y_m(k_{2,\perp} r) \right) \cos(m\phi)
\end{aligned} \tag{11}$$

where we have $k_{x,\perp} = \sqrt{n_x^2 k_0^2 - \beta^2}$. To determine the unknown coefficients, we will first use the boundary conditions of the electromagnetic field to relate the outer coefficients of A_2 , B_2 , C_2 and D_2 to the inner coefficients of A_1 and B_1 . We use that the tangential field components (E_z , H_z , E_ϕ and H_ϕ) are continuous across the interface:

$$\begin{aligned}
E_{1,z}(r=R, \phi) &= E_{2,z}(r=R, \phi) \\
E_{1,\phi}(r=R, \phi) &= E_{2,\phi}(r=R, \phi) \\
H_{1,z}(r=R, \phi) &= H_{2,z}(r=R, \phi) \\
H_{1,\phi}(r=R, \phi) &= H_{2,\phi}(r=R, \phi)
\end{aligned} \tag{12}$$

Inserting Eqs. (8-11) into Eq. (12) we obtain four equations with four unknowns and the following relations can be derived:

$$\begin{aligned}
A_2 &= \frac{A_1 K_2 + B_1 L_2}{k_0^2 n_2^2 T} \\
B_2 &= \frac{A_1 L_2 + B_1 K_1}{T} \\
C_2 &= -\frac{A_1 M_2 + B_1 L_1}{k_0^2 n_2^2 T} \\
D_2 &= -\frac{A_1 L_1 + B_1 M_1}{T}
\end{aligned} \tag{13}$$

where

$$\begin{aligned}
T &= \frac{2}{k_{2,\perp}^2 \beta R \pi} \\
L_1 &= \left(\frac{1}{k_{1,\perp}^2} - \frac{1}{k_{2,\perp}^2} \right) \frac{m}{R} J_m(k_{1,\perp} R) J_m(k_{2,\perp} R) \\
L_2 &= \left(\frac{1}{k_{1,\perp}^2} - \frac{1}{k_{2,\perp}^2} \right) \frac{m}{R} J_m(k_{1,\perp} R) Y_m(k_{2,\perp} R) \\
M_1 &= \frac{1}{\beta} \left(\frac{1}{k_{1,\perp}^2} \partial_{r=R} J_m(k_{1,\perp} r) J_m(k_{2,\perp} R) - \frac{1}{k_{2,\perp}^2} J_m(k_{1,\perp} R) \partial_{r=R} J_m(k_{2,\perp} r) \right) \\
M_2 &= \frac{1}{\beta} \left(\frac{k_0^2 n_1^2}{k_{1,\perp}^2} \partial_{r=R} J_m(k_{1,\perp} r) J_m(k_{2,\perp} R) - \frac{k_0^2 n_2^2}{k_{2,\perp}^2} J_m(k_{1,\perp} R) \partial_{r=R} J_m(k_{2,\perp} r) \right) \\
K_1 &= \frac{1}{\beta} \left(\frac{1}{k_{1,\perp}^2} \partial_{r=R} J_m(k_{1,\perp} r) Y_m(k_{2,\perp} R) - \frac{1}{k_{2,\perp}^2} J_m(k_{1,\perp} R) \partial_{r=R} Y_m(k_{2,\perp} r) \right) \\
K_2 &= \frac{1}{\beta} \left(\frac{k_0^2 n_1^2}{k_{1,\perp}^2} \partial_{r=R} J_m(k_{1,\perp} r) Y_m(k_{2,\perp} R) - \frac{k_0^2 n_2^2}{k_{2,\perp}^2} J_m(k_{1,\perp} R) \partial_{r=R} Y_m(k_{2,\perp} r) \right)
\end{aligned} \tag{14}$$

We now need to use the orthogonality condition for radiation modes and it is given by the following definition^{53,57-66}:

$$\int_S (\mathbf{E}_{p,s,m}(\mathbf{r}, k_\perp) \times \mathbf{H}_{p',s',m'}(\mathbf{r}, k'_\perp)) \cdot \hat{\mathbf{z}} dS = N_{p,s,m}(k_\perp) \delta_{p,p'} \delta_{s,s'} \delta_{m,m'} \delta(k_\perp - k'_\perp), \tag{15}$$

where p refers to the polarization discussed earlier (choosing either $\sin(m\phi)$ or $\cos(m\phi)$), s refers to the two orthogonal solutions and $N_{p,s,m}(k_\perp)$ is the normalization constant. We can split the normalization constant into the different parts: $N_{p,s,m}(k_\perp) = N_p N_m N_s(k_\perp)$. For

p we simply have $N_p = 1$ and we will generally omit this. For m we need to perform the ϕ integration involving either \cos or \sin :

$$\int_0^{2\pi} \cos(m\phi) \cos(m'\phi) d\phi = \begin{cases} 0 & m \neq m' \\ 2\pi & m = m' = 0 \\ \pi & m = m' \end{cases} \quad (16)$$

with the same result for \sin . We then obtain:

$$N_m = \begin{cases} 2\pi & m = 0 \\ \pi & m \geq 1 \end{cases} \quad (17)$$

For $N_s(k_\perp)$ we need to consider the radial integration, and only the terms which provides a delta function and these only appear for the outermost region (the air region). The only terms from Eq. (15) which provide a delta function are terms of the type:

$$\int_R^\infty J_{m+1}(k_\perp r) J_{m+1}(k'_\perp r) r dr = \frac{\delta(k_\perp - k'_\perp)}{k_\perp} + \text{finite terms} \quad (18)$$

and

$$\int_R^\infty Y_{m+1}(k_\perp r) Y_{m+1}(k'_\perp r) r dr = \frac{\delta(k_\perp - k'_\perp)}{k_\perp} + \text{finite terms} \quad (19)$$

It is commonly used that a delta function is obtained from Eq. (18)¹⁰⁵. It is less commonly used that a delta function is obtained from Eq. (19), however, referring to the supplementary of Ref.¹⁰⁶ the delta function is obtained. The final expression for Eq. (15) is then ($p = p'$):

$$\begin{aligned} & \int_0^\infty \int_0^{2\pi} (E_{r,s,m}(r, \phi, k_\perp) H_{\phi,s',m'}(r, \phi, k'_\perp) - E_{\phi,s,m}(r, \phi, k_\perp) H_{r,s',m'}(r, \phi, k'_\perp)) r d\phi dr = \\ & N_m \frac{\beta}{k_{2,\perp}^3} \left(k_0^2 n_2^2 A_{s,2} A_{s',2} + B_{s,2} B_{s',2} + k_0^2 n_2^2 C_{s,2} C_{s',2} + D_{s,2} D_{s',2} \right) \delta_{m,m'} \delta(k_\perp - k'_\perp) \end{aligned} \quad (20)$$

The two sets of orthogonal modes then need to satisfy:

$$k_0^2 n_2^2 A_{s,2} A_{s',2} + B_{s,2} B_{s',2} + k_0^2 n_2^2 C_{s,2} C_{s',2} + D_{s,2} D_{s',2} = 0 \quad (21)$$

There are infinitely many ways to choose the two sets of orthogonal modes, but to ensure $p_1(k_\perp) = 0$ we choose $A_{s=1,1} = 1$ with $B_{s=1,1} = -\beta$ which becomes apparent when considering Eq. (73). We then choose $A_{s=2,1} = 1$ with $B_{s=2,1} = \eta$. Using Eqs. (13-14) we then obtain:

$$\eta = -\frac{\beta Q_2 - Q_1}{\beta Q_3 - Q_2^2}, \quad (22)$$

where

$$\begin{aligned} Q_1 &= k_0^2 n_2^2 (L_1^2 + L_2^2) + K_2^2 + M_2^2 \\ Q_2 &= k_0^2 n_2^2 (K_1 L_2 + M_1 L_1) + K_2 L_2 + L_1 M_2 \\ Q_3 &= k_0^2 n_2^2 (K_1^2 + M_1^2) + L_1^2 + L_2^2 \end{aligned} \quad (23)$$

The normalization constant is then given by:

$$N = N_m \frac{\beta}{k_{2,\perp}^3} \left(k_0^2 n_2^2 A_{s,2}^2 + B_{s,2}^2 + k_0^2 n_2^2 C_{s,2}^2 + D_{s,2}^2 \right) \quad (24)$$

such that all coefficients are multiplied by $1/\sqrt{N}$.

10.3 Guided modes of infinite wire

For the guided modes, the solution is identical to the radiation modes in the wire region. However, in the air region the modified Bessel function is now the solution as $\beta > k_0 n_2$:

$$\begin{aligned} E_{2,z}(r, \phi) &= -i A_2 K_m(k_{2,g,\perp} r) \cos(m\phi) \\ H_{2,z}(r, \phi) &= -i B_2 K_m(k_{2,g,\perp} r) \sin(m\phi) \end{aligned} \quad (25)$$

where $k_{2,g,\perp} = \sqrt{\beta^2 - k_0^2 n_2^2}$. The k_{\perp} in Eq. (7) is now complex valued as $k_{\perp} = \sqrt{k_0^2 n_2^2 - \beta^2} = i\sqrt{\beta^2 - k_0^2 n_2^2} = ik_{2,g,\perp}$ such that there is a sign chance for the in-plane components of the electromagnetic field. The remaining components are then given by:

$$\begin{aligned} E_{2,r}(r, \phi) &= -\frac{\beta}{k_{2,g,\perp}^2} \left(B_2 \frac{m}{\beta} \frac{K_m(k_{2,g,\perp} r)}{r} + A_2 \partial_r K_m(k_{2,g,\perp} r) \right) \cos(m\phi) \\ E_{2,\phi}(r, \phi) &= \frac{\beta}{k_{2,g,\perp}^2} \left(A_2 m \frac{K_m(k_{2,g,\perp} r)}{r} + B_2 \frac{1}{\beta} \partial_r K_m(k_{2,g,\perp} r) \right) \sin(m\phi) \\ H_{2,r}(r, \phi) &= -\frac{\beta}{k_{2,g,\perp}^2} \left(A_2 m \frac{k_0^2 n_2^2}{\beta} \frac{K_m(k_{2,g,\perp} r)}{r} + B_2 \partial_r K_m(k_{2,g,\perp} r) \right) \sin(m\phi) \\ H_{2,\phi}(r, \phi) &= -\frac{\beta}{k_{2,g,\perp}^2} \left(B_2 m \frac{K_m(k_{2,g,\perp} r)}{r} + A_2 \frac{k_0^2 n_2^2}{\beta} \partial_r K_m(k_{2,g,\perp} r) \right) \cos(m\phi) \end{aligned} \quad (26)$$

Again we will use the boundary condition of Eq. (12) and obtain the following equation:

$$\begin{bmatrix} J_m(k_{1,\perp} R) & 0 & -K_m(k_{2,g,\perp} R) & 0 \\ 0 & J_m(k_{1,\perp} R) & 0 & -K_m(k_{2,g,\perp} R) \\ \frac{1}{k_{1,\perp}^2} \frac{m}{R} J_m(k_{1,\perp} R) & \frac{1}{k_{1,\perp}^2} \frac{1}{\beta} \partial_r J_m(k_{1,\perp} R) & \frac{1}{k_{2,g,\perp}^2} \frac{m}{R} K_m(k_{2,g,\perp} R) & \frac{1}{k_{2,g,\perp}^2} \frac{1}{\beta} \partial_r K_m(k_{2,g,\perp} R) \\ \frac{k_0^2 n_2^2}{k_{1,\perp}^2} \frac{1}{\beta} \partial_r J_m(k_{1,\perp} R) & \frac{1}{k_{1,\perp}^2} \frac{m}{R} J_m(k_{1,\perp} R) & \frac{k_0^2 n_2^2}{k_{2,g,\perp}^2} \frac{1}{\beta} \partial_r K_m(k_{2,g,\perp} R) & \frac{1}{k_{2,g,\perp}^2} \frac{m}{R} K_m(k_{2,g,\perp} R) \end{bmatrix} \begin{bmatrix} A_1 \\ B_1 \\ A_2 \\ B_2 \end{bmatrix} = 0 \quad (27)$$

To solve the equation, the determinant of the matrix must be 0, $\det(M(\beta)) = 0$, leading to the following transcendental equation:

$$\begin{aligned} J_m(k_{1,\perp} R)^2 \left(\frac{K_m(k_{2,g,\perp} R)}{\partial_r K_m(k_{2,g,\perp} R)} \right)^2 \beta^2 \frac{m^2}{R^2} (k_{1,\perp}^4 + k_{2,g,\perp}^4 + 2k_{1,\perp}^2 k_{2,g,\perp}^2) - k_{1,\perp}^4 k_0^2 n_2^2 J_m(k_{1,\perp} R)^2 \\ - k_{1,\perp}^2 k_{2,g,\perp}^2 (n_1^2 + n_2^2) k_0^2 \frac{K_m(k_{2,g,\perp} R)}{\partial_r K_m(k_{2,g,\perp} R)} J_m(k_{1,\perp} R) \partial_r J_m(k_{1,\perp} R) - k_{2,g,\perp}^4 k_0^2 n_1^2 \left(\frac{K_m(k_{2,g,\perp} R)}{\partial_r K_m(k_{2,g,\perp} R)} \right)^2 \partial_r J_m(k_{1,\perp} R)^2 = 0, \end{aligned} \quad (28)$$

where we have rearranged and scaled the terms to make the equation more robust when it is solved numerically. Having found the β , the coefficients can then be determined:

$$B_1 = 1$$

$$\begin{aligned} A_1 &= -B_1 \frac{k_{2,g,\perp}^2 \frac{\partial_r J_m(k_{1,\perp} R)}{J_m(k_{1,\perp} R)} + k_{1,\perp}^2 \frac{\partial_r K_m(k_{2,g,\perp} R)}{K_m(k_{2,g,\perp} R)}}{(k_{2,g,\perp}^2 + k_{1,\perp}^2) \beta \frac{m}{R}} \\ A_2 &= A_1 \frac{J_m(k_{1,\perp} R)}{K_m(k_{2,g,\perp} R)} \\ B_2 &= B_1 \frac{J_m(k_{1,\perp} R)}{K_m(k_{2,g,\perp} R)} \end{aligned} \quad (29)$$

We also need to normalize the guided modes and they fulfill the following orthogonality condition^{53,57–66}:

$$\int_S (\mathbf{E}_{p,n,m}(\mathbf{r}) \times \mathbf{H}_{p',n',m'}(\mathbf{r})) \cdot \hat{\mathbf{z}} dS = N_{p,n,m} \delta_{p,p'} \delta_{n,n'} \delta_{m,m'}, \quad (30)$$

where n is the mode number corresponding to the different solutions. Again we split up the normalization constant: $N_{p,n,m} = N_p N_n N_m$ with $N_p = 1$. For the azimuthal part we obtain the same result as in Eqs. (16-17) for the radiation modes. For the radial part we need to consider both the inner and outer part of Eq. (30). The inner part is:

$$N_{n,\text{inner}} = \frac{\beta^2}{k_{1,\perp}^4} \int_0^R \left(\frac{1}{\beta} (A_1^2 k_0^2 n_1^2 + B_1^2) \left(\frac{m^2}{r^2} J_m(k_{1,\perp} r)^2 + \partial_r J_m(k_{1,\perp} r)^2 \right) + 2A_1 B_1 \left(1 + \frac{k_0^2 n_1^2}{\beta} \right) \frac{m}{r} J_m(k_{1,\perp} r) \partial_r J_m(k_{1,\perp} r) \right) r dr \quad (31)$$

We now evaluate the two integrals appearing in Eq. (31) for $m = 1$:

$$\int_0^R \left(\frac{1}{r^2} J_1(kr)^2 + \partial_r J_1(kr)^2 \right) r dr = \frac{1}{2} \left(k^2 R^2 J_0(kR)^2 + (k^2 R^2 - 2) J_1(kR)^2 \right) \quad (32)$$

and

$$\int_0^R \left(\frac{1}{r} J_1(kr) \partial_r J_1(kr) \right) r dr = \frac{1}{2} J_1(kR)^2 \quad (33)$$

For the outer part we obtain:

$$N_{n,\text{outer}} = \frac{\beta^2}{k_{2,g,\perp}^4} \int_R^\infty \left(\frac{1}{\beta} (A_2^2 k_0^2 n_2^2 + B_2^2) \left(\frac{m^2}{r^2} K_m(k_{2,g,\perp} r)^2 + \partial_r K_m(k_{2,g,\perp} r)^2 \right) + 2A_2 B_2 \left(1 + \frac{k_0^2 n_2^2}{\beta} \right) \frac{m}{r} K_m(k_{2,g,\perp} r) \partial_r K_m(k_{2,g,\perp} r) \right) r dr \quad (34)$$

We now evaluate the two integrals appearing in Eq. (34) for $m = 1$:

$$\begin{aligned} \int_R^\infty \left(\frac{1}{r^2} K_1(kr)^2 + \partial_r K_1(kr)^2 \right) r dr &= \\ \frac{k^2 R^2}{2} (K_1(kR)^2 - K_0(kR)^2) + K_1(kR)^2 & \end{aligned} \quad (35)$$

and

$$\int_R^\infty \left(\frac{1}{r} K_1(kr) \partial_r K_1(kr) \right) r dr = -\frac{1}{2} K_1(kR)^2 \quad (36)$$

The normalization constant is then given by:

$$N = N_m (N_{n,\text{inner}} + N_{n,\text{outer}}) \quad (37)$$

such that all coefficients are multiplied by $1/\sqrt{N}$. The radiation modes and guided modes are also orthogonal to each other^{53,57–66}:

$$\int_S (\mathbf{E}_{p,s,m}(\mathbf{r}, k_{\perp}) \times \mathbf{H}_{p',n',m'}(\mathbf{r})) \cdot \hat{\mathbf{z}} dS = 0 \quad (38)$$

10.4 Radiation modes of a multilayered cylindrical structure

For the structure with many radial layers we will employ the transfer-matrix formalism⁵⁵. In the inner region, the solution to the z -components is identical to Eq. (8) while in all other layers, Eq. (8) is the solution. We then connect the fields at the interfaces and ultimately, the outer coefficients can be related to the inner coefficients:

$$T \begin{bmatrix} A_1 \\ B_1 \end{bmatrix} = \begin{bmatrix} A_N \\ B_N \\ C_N \\ D_N \end{bmatrix}. \quad (39)$$

We will now describe how the matrix T is obtained. The boundary conditions at the first interface gives the following equation:

$$M_1(R_1) \begin{bmatrix} A_1 \\ B_1 \end{bmatrix} = M_2(R_1) \begin{bmatrix} A_2 \\ B_2 \\ C_2 \\ D_2 \end{bmatrix}. \quad (40)$$

At the second interface we have:

$$M_2(R_2) \begin{bmatrix} A_2 \\ B_2 \\ C_2 \\ D_2 \end{bmatrix} = M_3(R_2) \begin{bmatrix} A_3 \\ B_3 \\ C_3 \\ D_3 \end{bmatrix}. \quad (41)$$

In this way we can obtain:

$$M_3(R_2)^{-1} M_2(R_2) M_2(R_1)^{-1} M_1(R_1) \begin{bmatrix} A_1 \\ B_1 \end{bmatrix} = \begin{bmatrix} A_3 \\ B_3 \\ C_3 \\ D_3 \end{bmatrix}. \quad (42)$$

And for N layers:

$$M_N(R_{N-1})^{-1} M_{N-1}(R_{N-1}) \dots M_2(R_2) M_2(R_1)^{-1} M_1(R_1) \begin{bmatrix} A_1 \\ B_1 \end{bmatrix} = \begin{bmatrix} A_N \\ B_N \\ C_N \\ D_N \end{bmatrix}. \quad (43)$$

The very first matrix is given by:

$$M_1(R_1) = \begin{bmatrix} J_m(k_{1,\perp} R_1) & 0 \\ 0 & J_m(k_{1,\perp} R_1) \\ \frac{1}{k_{1,\perp}^2} \frac{m}{R_1} J_m(k_{1,\perp} R_1) & \frac{1}{k_{1,\perp}^2} \frac{1}{\beta} \partial_r J_m(k_{1,\perp} R_1) \\ \frac{k_0^2 n_1^2}{k_{1,\perp}^2} \frac{1}{\beta} \partial_r J_m(k_{1,\perp} R_1) & \frac{1}{k_{1,\perp}^2} \frac{m}{R_1} J_m(k_{1,\perp} R_1) \end{bmatrix}. \quad (44)$$

while the remaining matrices are given by:

$$M_n(R_x) = \begin{bmatrix} J_m(k_{n,\perp}R_x) & 0 & Y_m(k_{n,\perp}R_x) & 0 \\ 0 & J_m(k_{n,\perp}R_x) & 0 & J_m(k_{n,\perp}R_x) \\ \frac{1}{k_{n,\perp}^2} \frac{m}{R_x} J_m(k_{n,\perp}R_x) & \frac{1}{k_{n,\perp}^2} \frac{1}{\beta} \partial_r J_m(k_{n,\perp}R_x) & \frac{1}{k_{n,\perp}^2} \frac{m}{R_x} Y_m(k_{n,\perp}R_x) & \frac{1}{k_{n,\perp}^2} \frac{1}{\beta} \partial_r Y_m(k_{n,\perp}R_x) \\ \frac{k_0^2 n_n^2}{k_{n,\perp}^2} \frac{1}{\beta} \partial_r J_m(k_{n,\perp}R_x) & \frac{1}{k_{n,\perp}^2} \frac{m}{R_x} J_m(k_{n,\perp}R_x) & \frac{k_0^2 n_n^2}{k_{n,\perp}^2} \frac{1}{\beta} \partial_r Y_m(k_{n,\perp}R_x) & \frac{1}{k_{n,\perp}^2} \frac{m}{R_x} Y_m(k_{n,\perp}R_x) \end{bmatrix}. \quad (45)$$

and the inverse:

$$M_n(R_x)^{-1} = \frac{\pi}{2} \begin{bmatrix} R_x \partial_r Y_m(k_{n,\perp}R_x) & m \frac{\beta}{k_0^2 n_n^2} Y_m(k_{n,\perp}R_x) & 0 & -R_x \frac{\beta k_{n,\perp}^2}{k_0^2 n_n^2} Y_m(k_{n,\perp}R_x) \\ m \beta Y_m(k_{n,\perp}R_x) & R_x \partial_r Y_m(k_{n,\perp}R_x) & -R_x \beta k_{n,\perp}^2 Y_m(k_{n,\perp}R_x) & 0 \\ -R_x \partial_r J_m(k_{n,\perp}R_x) & -m \frac{\beta}{k_0^2 n_n^2} J_m(k_{n,\perp}R_x) & 0 & R_x \frac{\beta k_{n,\perp}^2}{k_0^2 n_n^2} J_m(k_{n,\perp}R_x) \\ -m \beta J_m(k_{n,\perp}R_x) & -R_x \partial_r J_m(k_{n,\perp}R_x) & R_x \beta k_{n,\perp}^2 J_m(k_{n,\perp}R_x) & 0 \end{bmatrix}. \quad (46)$$

Again we will use $A_{s=1,1} = 1$ with $B_{s=1,1} = -\beta$ and $A_{s=2,1} = 1$ with $B_{s=2,1} = \eta$. η is now given by:

$$\eta = \frac{P_1 - \beta P_2}{\beta P_3 - P_2}, \quad (47)$$

where

$$\begin{aligned} P_1 &= k_0^2 n_N^2 (T_{1,1}^2 + T_{3,1}^2) + T_{2,1}^2 + T_{4,1}^2 \\ P_2 &= k_0^2 n_N^2 (T_{1,1} T_{1,2} + T_{3,2} T_{3,1}) + T_{2,1} T_{2,2} + T_{4,1} T_{4,2} \\ P_3 &= k_0^2 n_N^2 (T_{1,2}^2 + T_{3,2}^2) + T_{2,2}^2 + T_{4,2}^2 \end{aligned} \quad (48)$$

$T_{q,q'}$ are the matrix elements of the matrix T . We generally assume that the surrounding medium is air: $n_N = 1$. We then normalize the modes exactly the same way as for the wire.

10.5 Guided modes of a multilayered cylindrical structure

For the guided modes of the cylindrical structure we use a similar method as in^{96,97} and build one large matrix to obtain the following equation:

$$M_G \begin{bmatrix} A_1 \\ B_1 \\ \vdots \\ A_N \\ B_N \end{bmatrix} = 0, \quad (49)$$

where M_G has dimensions of $4(N-1) \times 4(N-1)$. In the following we assume that the layers consist of alternating layers of two different materials with two different refractive index. We assume that the wire region consists of the large refractive index material and that the outer most layer consists of the low refractive index material. However, the following method can easily be applied to structures with many different materials. In the large refractive index regions the solutions are $J_m(k_{1,\perp}r)$ and $Y_m(k_{1,\perp}r)$, except in the inner wire region where only $J_m(k_{1,\perp}r)$ is allowed. In the low refractive index regions the solutions are $K_m(k_{2,g,\perp}r)$ and $I_m(k_{2,g,\perp}r)$, except in the outer most region where only $K_m(k_{2,g,\perp}r)$ is allowed. Initially, all elements of M_G are 0 and we then need to fill out the elements accordingly. We will use the following scaling to the coefficients in the low index regions: $A_x = k_{2,g,\perp}^2 / \partial_r K_m(k_{2,g,\perp}R_{x-1}) A'_x$ (same for B_x) and $C_x = k_{2,g,\perp}^2 / \partial_r I_m(k_{2,g,\perp}R_x) C'_x$ (same for D_x). We found that this scaling made the method much more numerically stable. The first submatrix, $M_{G,1-4,1-6}$, can be determined by considering the first boundary:

$$\begin{bmatrix} J_m(k_{1,\perp} R_1) & 0 & -k_{2,g,\perp}^2 \frac{K_m(k_{2,g,\perp} R_1)}{\partial_r K_m(k_{2,g,\perp} R_1)} & 0 & -k_{2,g,\perp}^2 \frac{I_m(k_{2,g,\perp} R_1)}{\partial_r I_m(k_{2,g,\perp} R_2)} & 0 \\ 0 & J_m(k_{1,\perp} R_1) & 0 & -k_{2,g,\perp}^2 \frac{K_m(k_{2,g,\perp} R_1)}{\partial_r K_m(k_{2,g,\perp} R_1)} & 0 & -k_{2,g,\perp}^2 \frac{I_m(k_{2,g,\perp} R_1)}{\partial_r I_m(k_{2,g,\perp} R_2)} \\ \frac{\beta}{k_{1,\perp}^2} \frac{m}{R_1} J_m(k_{1,\perp} R_1) & \frac{1}{k_{1,\perp}^2} \partial_r J_m(k_{1,\perp} R_1) & \beta \frac{m}{R_1} \frac{K_m(k_{2,g,\perp} R_1)}{\partial_r K_m(k_{2,g,\perp} R_1)} & 1 & \beta \frac{m}{R_1} \frac{I_m(k_{2,g,\perp} R_1)}{\partial_r I_m(k_{2,g,\perp} R_2)} & \beta \frac{m}{R_1} \frac{I_m(k_{2,g,\perp} R_1)}{\partial_r I_m(k_{2,g,\perp} R_2)} \\ \frac{k_0^2 n_1^2}{k_{1,\perp}^2} \partial_r J_m(k_{1,\perp} R_1) & \frac{\beta}{k_{1,\perp}^2} \frac{m}{R_1} J_m(k_{1,\perp} R_1) & k_0^2 n_2^2 & \beta \frac{m}{R_1} \frac{K_m(k_{2,g,\perp} R_1)}{\partial_r K_m(k_{2,g,\perp} R_1)} & k_0^2 n_2^2 \frac{\partial_r J_m(k_{2,g,\perp} R_1)}{\partial_r I_m(k_{2,g,\perp} R_2)} & \beta \frac{m}{R_1} \frac{I_m(k_{2,g,\perp} R_1)}{\partial_r I_m(k_{2,g,\perp} R_2)} \end{bmatrix} \begin{bmatrix} A_1 \\ B_1 \\ A'_2 \\ B'_2 \\ C'_2 \\ D'_2 \end{bmatrix} = 0 \quad (50)$$

At the second interface, we obtain the submatrix, $M_{G,5-8,3-10}$:

$$\begin{bmatrix} -k_{2,g,\perp}^2 \frac{K_m(k_{2,g,\perp} R_2)}{\partial_r K_m(k_{2,g,\perp} R_1)} & 0 & -k_{2,g,\perp}^2 \frac{I_m(k_{2,g,\perp} R_2)}{\partial_r I_m(k_{2,g,\perp} R_2)} & 0 & J_m(k_{1,\perp} R_2) & 0 & Y_m(k_{1,\perp} R_2) & 0 \\ 0 & -k_{2,g,\perp}^2 \frac{K_m(k_{2,g,\perp} R_2)}{\partial_r K_m(k_{2,g,\perp} R_1)} & 0 & -k_{2,g,\perp}^2 \frac{I_m(k_{2,g,\perp} R_2)}{\partial_r I_m(k_{2,g,\perp} R_2)} & 0 & J_m(k_{1,\perp} R_2) & 0 & Y_m(k_{1,\perp} R_2) \\ \beta \frac{m}{R_2} \frac{K_m(k_{2,g,\perp} R_2)}{\partial_r K_m(k_{2,g,\perp} R_1)} & \frac{1}{k_{1,\perp}^2} \frac{m}{R_2} J_m(k_{1,\perp} R_2) & \beta \frac{m}{R_2} \frac{I_m(k_{2,g,\perp} R_2)}{\partial_r I_m(k_{2,g,\perp} R_2)} & 1 & \frac{\beta}{k_{1,\perp}^2} \frac{m}{R_2} J_m(k_{1,\perp} R_2) & \frac{1}{k_{1,\perp}^2} \frac{m}{R_2} \partial_r J_m(k_{1,\perp} R_2) & \frac{\beta}{k_{1,\perp}^2} \frac{m}{R_2} Y_m(k_{1,\perp} R_2) & \frac{1}{k_{1,\perp}^2} \partial_r Y_m(k_{1,\perp} R_2) \\ k_0^2 n_2^2 \frac{\partial_r K_m(k_{2,g,\perp} R_2)}{\partial_r K_m(k_{2,g,\perp} R_1)} & \beta \frac{m}{R_2} \frac{K_m(k_{2,g,\perp} R_2)}{\partial_r K_m(k_{2,g,\perp} R_1)} & k_0^2 n_2^2 & \beta \frac{m}{R_2} \frac{I_m(k_{2,g,\perp} R_2)}{\partial_r I_m(k_{2,g,\perp} R_2)} & k_0^2 n_2^2 \frac{\partial_r J_m(k_{1,\perp} R_2)}{\partial_r I_m(k_{1,\perp} R_2)} & \frac{\beta}{k_{1,\perp}^2} \frac{m}{R_2} J_m(k_{1,\perp} R_2) & \frac{\beta}{k_{1,\perp}^2} \frac{m}{R_2} \partial_r Y_m(k_{1,\perp} R_2) & \frac{\beta}{k_{1,\perp}^2} \frac{m}{R_2} Y_m(k_{1,\perp} R_2) \end{bmatrix} \begin{bmatrix} A'_2 \\ B'_2 \\ C'_2 \\ D'_2 \\ A_3 \\ B_3 \\ C_3 \\ D_3 \end{bmatrix} = 0 \quad (51)$$

At the third interface we would simply need to switch around the two 4X4 submatrices in Eq. (51) and adjust the radii inputs. At each interface (besides the first and last), x , we thus obtain the submatrix $M_{G,(5+4(x-1))-(5+4(x-1)+3),(3+4(x-1))-(3+4(x-1)+7)}$. At the last interface we obtain the submatrix, $M_{G,(5+4(N-3))-(5+4(N-3)+3),(3+4(N-3))-(4(N-1))}$:

$$\begin{bmatrix} J_m(k_{1,\perp} R_{N-1}) & 0 & Y_m(k_{1,\perp} R_{N-1}) & 0 & -k_{2,g,\perp}^2 \frac{K_m(k_{2,g,\perp} R_{N-1})}{\partial_r K_m(k_{2,g,\perp} R_{N-1})} & 0 \\ 0 & J_m(k_{1,\perp} R_{N-1}) & 0 & Y_m(k_{1,\perp} R_{N-1}) & 0 & -k_{2,g,\perp}^2 \frac{K_m(k_{2,g,\perp} R_{N-1})}{\partial_r K_m(k_{2,g,\perp} R_{N-1})} \\ \frac{\beta}{k_{1,\perp}^2} \frac{m}{R_{N-1}} J_m(k_{1,\perp} R_{N-1}) & \frac{1}{k_{1,\perp}^2} \partial_r J_m(k_{1,\perp} R_{N-1}) & \frac{\beta}{k_{1,\perp}^2} \frac{m}{R_{N-1}} Y_m(k_{1,\perp} R_{N-1}) & \frac{1}{k_{1,\perp}^2} \partial_r Y_m(k_{1,\perp} R_{N-1}) & \beta \frac{m}{R_{N-1}} \frac{K_m(k_{2,g,\perp} R_{N-1})}{\partial_r K_m(k_{2,g,\perp} R_{N-1})} & 1 \\ \frac{k_0^2 n_1^2}{k_{1,\perp}^2} \partial_r J_m(k_{1,\perp} R_{N-1}) & \frac{\beta}{k_{1,\perp}^2} \frac{m}{R_{N-1}} J_m(k_{1,\perp} R_{N-1}) & \frac{k_0^2 n_1^2}{k_{1,\perp}^2} \partial_r Y_m(k_{1,\perp} R_{N-1}) & \frac{\beta}{k_{1,\perp}^2} \frac{m}{R_{N-1}} Y_m(k_{1,\perp} R_{N-1}) & k_0^2 n_2^2 & \beta \frac{m}{R_{N-1}} \frac{K_m(k_{2,g,\perp} R_{N-1})}{\partial_r K_m(k_{2,g,\perp} R_{N-1})} \end{bmatrix} \begin{bmatrix} A_{N-1} \\ B_{N-1} \\ C_{N-1} \\ D_{N-1} \\ A'_N \\ B'_N \end{bmatrix} = 0 \quad (52)$$

Then we find the solutions, $\det(M_G(\beta)) = 0$, and use MATLAB to determine the coefficients and we can easily scale back. Finally, the guided modes of the cylindrical structures also needs to be normalized. For the inner and outer most regions we can reuse the result from the wire. For the remaining regions we need to calculate the different integrals and in the high index regions we obtain:

$$N_{n,x,\text{high index}} =$$

$$\begin{aligned} & \frac{\beta^2}{k_{1,\perp}^4} \int_{R_{x-1}}^{R_x} \left(\frac{1}{\beta} (A_x^2 k_0^2 n_1^2 + B_x^2) \left(\frac{m^2}{r^2} J_m(k_{1,\perp} r)^2 + \partial_r J_m(k_{1,\perp} r)^2 \right) + 2A_x B_x (1 + \frac{k_0^2 n_1^2}{\beta}) \frac{m}{r} J_m(k_{1,\perp} r) \partial_r J_m(k_{1,\perp} r) + \right. \\ & \frac{1}{\beta} (C_x^2 k_0^2 n_1^2 + D_x^2) \left(\frac{m^2}{r^2} Y_m(k_{1,\perp} r)^2 + \partial_r Y_m(k_{1,\perp} r)^2 \right) + 2C_x D_x (1 + \frac{k_0^2 n_1^2}{\beta}) \frac{m}{r} Y_m(k_{1,\perp} r) \partial_r Y_m(k_{1,\perp} r) + \\ & \left. \frac{2}{\beta} (A_x C_x k_0^2 n_1^2 + B_x D_x) \left(\frac{m^2}{r^2} J_m(k_{1,\perp} r) Y_m(k_{1,\perp} r) + \partial_r J_m(k_{1,\perp} r) \partial_r Y_m(k_{1,\perp} r) \right) + \right. \\ & \left. (A_x D_x + B_x C_x) (1 + \frac{k_0^2 n_1^2}{\beta}) \frac{m}{r} (\partial_r J_m(k_{1,\perp} r) Y_m(k_{1,\perp} r) + J_m(k_{1,\perp} r) \partial_r Y_m(k_{1,\perp} r)) \right) r dr \end{aligned} \quad (53)$$

We will now evaluate all the integrals for $m = 1$:

$$\begin{aligned}
& \int_a^b \left(\frac{1}{r^2} J_1(kr)^2 + \partial_r J_1(kr)^2 \right) r dr = \\
& \frac{1}{2} ((2 - a^2 k^2) J_1(ka)^2 + (b^2 k^2 - 2) J_1(kb)^2 - a^2 k^2 J_0(ka)^2 + b^2 k^2 J_0(kb)^2)
\end{aligned} \tag{54}$$

and

$$\int_a^b \left(\frac{1}{r} J_1(kr) \partial_r J_1(kr) \right) r dr = \frac{1}{2} (J_1(kb)^2 - J_1(ka)^2) \tag{55}$$

and

$$\begin{aligned}
& \int_a^b \left(\frac{1}{r^2} Y_1(kr)^2 + \partial_r Y_1(kr)^2 \right) r dr = \\
& \frac{1}{2} ((2 - a^2 k^2) Y_1(ka)^2 + (b^2 k^2 - 2) Y_1(kb)^2 - a^2 k^2 Y_0(ka)^2 + b^2 k^2 Y_0(kb)^2)
\end{aligned} \tag{56}$$

and

$$\int_a^b \left(\frac{1}{r} Y_1(kr) \partial_r Y_1(kr) \right) r dr = \frac{1}{2} (Y_1(kb)^2 - Y_1(ka)^2) \tag{57}$$

and

$$\begin{aligned}
& \int_a^b \left(\frac{1}{r^2} J_1(kr) Y_1(kr) + \partial_r J_1(kr) \partial_r Y_1(kr) \right) r dr = \\
& \frac{k^2}{2} (b^2 J_1(kb) Y_1(kb) + b^2 J_0(kb) Y_0(kb) - a^2 J_1(ka) Y_1(ka) - a^2 J_0(ka) Y_0(ka)) + J_1(ka) Y_1(ka) - J_1(kb) Y_1(kb)
\end{aligned} \tag{58}$$

and

$$\int_a^b \left(\frac{1}{r} \partial_r J_1(kr) Y_1(kr) + \frac{1}{r} J_1(kr) \partial_r Y_1(kr) \right) r dr = J_1(kb) Y_1(kb) - J_1(ka) Y_1(k_{1,\perp} a) \tag{59}$$

For the low index regions we obtain:

$$\begin{aligned}
N_{n,x,\text{low index}} = & \\
& \frac{\beta^2}{k_{2,g,\perp}^4} \int_{R_{x-1}}^{R_x} \left(\frac{1}{\beta} (A_x^2 k_0^2 n_2^2 + B_x^2) \left(\frac{m^2}{r^2} K_m(k_{2,g,\perp} r)^2 + \partial_r K_m(k_{2,g,\perp} r)^2 \right) + 2A_x B_x (1 + \frac{k_0^2 n_2^2}{\beta}) \frac{m}{r} K_m(k_{2,g,\perp} r) \partial_r K_m(k_{2,g,\perp} r) + \right. \\
& \frac{1}{\beta} (C_x^2 k_0^2 n_2^2 + D_x^2) \left(\frac{m^2}{r^2} I_m(k_{2,g,\perp} r)^2 + \partial_r I_m(k_{2,g,\perp} r)^2 \right) + 2C_x D_x (1 + \frac{k_0^2 n_1^2}{\beta}) \frac{m}{r} I_m(k_{2,g,\perp} r) \partial_r I_m(k_{2,g,\perp} r) + \\
& \frac{2}{\beta} (A_x C_x k_0^2 n_2^2 + B_x D_x) \left(\frac{m^2}{r^2} K_m(k_{2,g,\perp} r) I_m(k_{2,g,\perp} r) + \partial_r K_m(k_{2,g,\perp} r) \partial_r I_m(k_{2,g,\perp} r) \right) \\
& \left. + (A_x D_x + B_x C_x) (1 + \frac{k_0^2 n_2^2}{\beta}) \frac{m}{r} (\partial_r K_m(k_{2,g,\perp} r) I_m(k_{2,g,\perp} r) + K_m(k_{2,g,\perp} r) \partial_r I_m(k_{2,g,\perp} r)) \right) r dr
\end{aligned} \tag{60}$$

Again, we will evaluate all integrals for $m = 1$:

$$\begin{aligned} \int_a^b \left(\frac{1}{r^2} K_1(kr)^2 + \partial_r K_1(kr)^2 \right) r dr = \\ \frac{k^2}{2} (a^2(K_1(ka)^2 - K_0(ka)^2) - b^2(K_1(kb)^2 - K_0(kb)^2)) - (K_1(kb)^2 - K_1(ka)^2) \end{aligned} \quad (61)$$

and

$$\int_a^b \left(\frac{1}{r} K_1(kr) \partial_r K_1(kr) \right) r dr = \frac{1}{2} (K_1(kb)^2 - K_1(ka)^2) \quad (62)$$

and

$$\begin{aligned} \int_a^b \left(\frac{1}{r^2} I_1(kr)^2 + \partial_r I_1(kr)^2 \right) r dr = \\ \frac{1}{2} ((2 + a^2 k^2) I_1(ka)^2 - (2 + b^2 k^2) I_1(kb)^2 - a^2 k^2 I_0(ka)^2 + b^2 k^2 I_0(kb)^2) \end{aligned} \quad (63)$$

and

$$\int_a^b \left(\frac{1}{r} I_1(kr) \partial_r I_1(kr) \right) r dr = \frac{1}{2} (I_1(kb)^2 - I_1(ka)^2) \quad (64)$$

and

$$\begin{aligned} \int_a^b \left(\frac{1}{r^2} K_1(kr) I_1(kr) + \partial_r K_1(kr) \partial_r I_1(kr) \right) r dr = \\ \frac{k^2}{2} (a^2(K_1(ka)I_1(ka) + K_0(ka)I_0(ka)) - b^2(K_1(kb)I_1(kb) + K_0(kb)I_0(kb))) - (K_1(kb)I_1(kb) - K_1(ka)I_1(ka)) \end{aligned} \quad (65)$$

and

$$\begin{aligned} \int_a^b \left(\frac{1}{r} \partial_r K_1(kr) I_1(kr) + \frac{1}{r} K_1(kr) \partial_r I_1(kr) \right) r dr = \\ K_1(kb)I_1(kb) - K_1(ka)I_1(ka) \end{aligned} \quad (66)$$

All the contributions can then be added together and the normalization constant is then calculated.

10.6 Expansion coefficients and power emission

The electrical emitted by a dipole is expanded upon the eigenmodes and the electrical field above (+) and below (-) the dipole is (assuming the dipole is placed at $z = 0$):

$$\mathbf{E}^\pm(r, \phi, z) = \sum_{n=1}^N a_{n,m}^\pm \mathbf{e}_{n,m}^\pm(r, \phi) \exp(\pm i \beta_{n,m} z) + \sum_{s=1}^2 \int_0^\infty a_{s,m}^\pm(k_\perp) \mathbf{e}_{s,m}^\pm(r, \phi, k_\perp) \exp(\pm i \beta(k_\perp) z) dk_\perp, \quad (67)$$

where we have, $\mathbf{e}_\perp^- = \mathbf{e}_\perp^+$ and $\mathbf{e}_z^- = -\mathbf{e}_z^+$ ⁵⁴. In the above derivations of the eigenmodes we considered (+). The field amplitudes are derived from the Lorentz reciprocity theorem. For the guided modes they are given by⁵³:

$$a_{n,m}^\pm = -\omega \mu_0 \frac{1}{2} \int_V \mathbf{J}(\mathbf{r}) \cdot \mathbf{e}_{n,m}^\mp(r, \phi) dV. \quad (68)$$

$\omega\mu_0$ now appear due the scaling of the magnetic field. The associated current distribution for a point dipole is given by: $\mathbf{J}(\mathbf{r}) = -i\omega\mathbf{p}\delta(\mathbf{r} - \mathbf{r}_d)$. The dipole is placed on axis and is polarized along the x-direction which results in, $\mathbf{r}_d = [0, 0, 0]$ and $\mathbf{p} = |\mathbf{p}|[1, 0, 0]$. Inserting this into Eq. (68) we obtain:

$$a_{n,m=1}^{\pm} = \frac{1}{2}i\omega^2\mu_0|\mathbf{p}|e_{r,n,m=1}^{\mp}(r=0, \phi=0) = \frac{1}{4k_{\perp,n}}i\omega^2\mu_0|\mathbf{p}|\frac{\beta_n A_{1,n} + B_{1,n}}{\sqrt{N_{g,n}}}. \quad (69)$$

The field amplitudes for the radiation modes are given by⁵³:

$$a_{s,m}^{\pm}(k_{\perp}) = -\omega\mu_0\frac{1}{2}\int_V \mathbf{J}(\mathbf{r}) \cdot \mathbf{e}_{s,m}^{\mp}(r, \phi, k_{\perp}) dV = \frac{1}{4k_{\perp}}i\omega^2\mu_0|\mathbf{p}|\frac{\beta(k_{\perp})A_{1,s}(k_{\perp}) + B_{1,s}(k_{\perp})}{\sqrt{N_s(k_{\perp})}} \quad (70)$$

The emitted power is given by⁵²:

$$P = -\frac{1}{2}\int_V \text{Re}[\mathbf{J}^*(\mathbf{r}) \cdot \mathbf{E}^+(\mathbf{r})] dV. \quad (71)$$

For the guided modes we obtain:

$$\begin{aligned} P_G &= -\frac{1}{2}\sum_{n=1}^N \text{Re}[i\omega a_n^+ \mathbf{p} \cdot \mathbf{e}_n^+(r=0, \phi=0)] = -\frac{1}{2}\sum_{n=1}^N \text{Re}[i\omega\mu_0\frac{1}{4k_{\perp,n}}i\omega|\mathbf{p}|\frac{\beta_n A_{1,n} + B_{1,n}}{\sqrt{N_{g,n}}}|\mathbf{p}|\frac{1}{2k_{\perp,n}}\frac{\beta_n A_{1,n} + B_{1,n}}{\sqrt{N_{g,n}}}] \\ &= \frac{1}{16}\omega^3\mu_0|\mathbf{p}|^2\sum_{n=1}^N \frac{(\beta_n A_{1,n} + B_{1,n})^2}{k_{\perp,n}^2 N_{g,n}} = \sum_{n=1}^N P_{g,n} \end{aligned} \quad (72)$$

For the radiation modes we obtain:

$$\begin{aligned} P_R &= -\frac{1}{2}\sum_{s=1}^2 \int_0^{\infty} \text{Re}[i\omega a_s^+(k_{\perp}) \mathbf{p} \cdot \mathbf{e}_s^+(r=0, \phi=0, k_{\perp})] dk_{\perp} \\ &= -\frac{1}{2}\sum_{s=1}^2 \int_0^{\infty} \text{Re}[i\omega^2\mu_0\frac{1}{4k_{\perp}}i\omega|\mathbf{p}|\frac{\beta(k_{\perp})A_{1,s}(k_{\perp}) + B_{1,s}(k_{\perp})}{\sqrt{N_s(k_{\perp})}}|\mathbf{p}|\frac{1}{2k_{\perp}}\frac{\beta(k_{\perp})A_{1,s}(k_{\perp}) + B_{1,s}(k_{\perp})}{\sqrt{N_s(k_{\perp})}}] dk_{\perp} \\ &= \frac{1}{16}\omega^3\mu_0|\mathbf{p}|^2\sum_{s=1}^2 \int_0^{\infty} \text{Re}[\frac{(\beta(k_{\perp})A_{1,s}(k_{\perp}) + B_{1,s}(k_{\perp}))^2}{k_{\perp}^2 N_s(k_{\perp})}] dk_{\perp} = \frac{1}{16}\omega^3\mu_0|\mathbf{p}|^2\sum_{s=1}^2 \int_0^{k_0} \frac{(\beta(k_{\perp})A_{1,s}(k_{\perp}) + B_{1,s}(k_{\perp}))^2}{k_{\perp}^2 N_s(k_{\perp})} dk_{\perp} \end{aligned} \quad (73)$$

We can then define:

$$P_R = \sum_{s=1}^2 \int_0^{k_0} p_s(k_{\perp}) dk_{\perp}. \quad (74)$$

The emitted power in a bulk medium is given by⁵²:

$$P_0 = \frac{1}{12\pi}\omega^3\mu_0|\mathbf{p}|^2 n_{\text{bulk}} k_0 \quad (75)$$

10.7 Numerical challenges for more than 1 ring

When adding more rings around the wire we encountered a numerical challenge using the analytical method. To illustrate this challenge we have plotted the total emission, P_T/P_0 , in Fig. (17a) for a wire with $D = 0.9832 \mu\text{m}$ surrounded by two rings with identical air gaps and ring thicknesses such that $r_1 = r_3$ and $r_2 = r_4$.

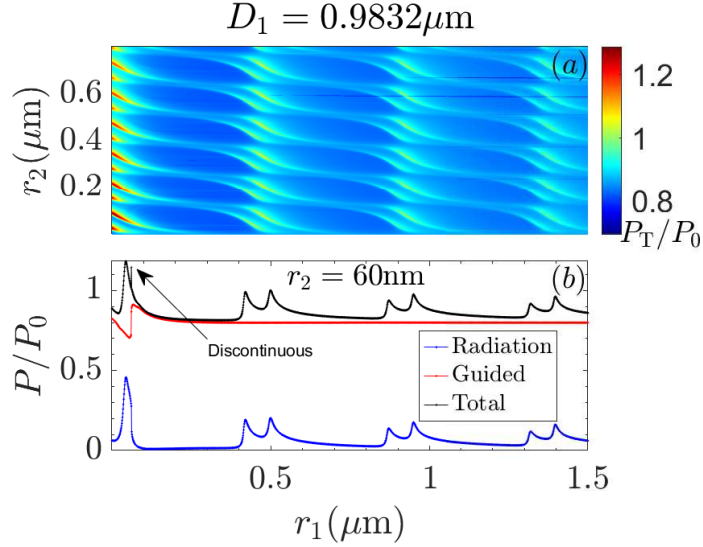


Fig. 17 (a) P_T/P_0 as a function of the air gap, r_1 and ring thickness, r_2 , for $D = 0.9832\mu\text{m}$ with 2 rings with identical air gaps and ring thicknesses. For the largest values of r_1 and r_2 a few lines can be seen where the guided modes were not located leading to discontinuities. (b) P_R/P_0 , P_G/P_0 and P_T/P_0 as a function of the air gap, r_1 , with ring thicknesses of $r_2 = 60\text{nm}$. The arrow indicates where P_T/P_0 is discontinuous.

Here the total emission rate is no longer always continuous at the onset of a new guided mode. This can be seen in Fig. (17b), where P_T/P_0 spikes up for one data point exactly at the onset of a new guided mode, because the emission rate into radiation modes has not yet dropped. This is mostly likely due to numerical limitations and the exact transition point between radiation modes and guided modes would probably be problematic for any numerical algorithm⁹⁹. The opposite can also occur, where P_T/P_0 drops as the emission rate into radiation modes drops just before the onset of a new guided mode. This issue is generally not a problem as P_T/P_0 is still continuous for most parameters, but using the analytical method exactly at the onset of new guided mode should be done with caution.

However, in the optimization of the β factor the discontinuity of P_T/P_0 at the onset of new guided modes is problematic as this can lead to nonphysical peaks in the β factor which the optimization procedure could locate. Therefore we have implemented two different kinds of constraints (see the next subsection) with the purpose of avoiding these points and used 2-3 optimization algorithms in MATLAB. The result is shown in Fig. (18). This does not lead to a completely smooth curve for the β factor as for one ring, but we can confidently determine that within a limited interval the β factor can be further increased.

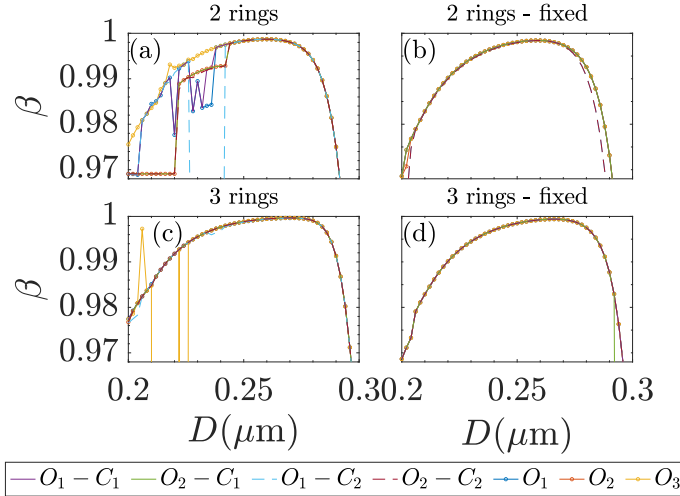


Fig. 18 Optimized β factor as a function of the wire diameter for 2 rings (a), 2 rings with fixed parameters (b), 3 rings (c) and 3 rings with fixed parameters (d). In each subplot, there are 7 curves indicated by the legend. O corresponds to the optimization algorithm, either 1, 2 or 3. C corresponds to the constraint either 1 or 2 and without any C there is no constraint.

For most diameters, the different optimizations with and without constraints find the same value for the β factor showing that the results are reliable. To construct Fig. (8), we have chosen the values which leads to smooth curves for the β factor.

10.8 Optimization and constraints in the β -factor optimization

In the β -factor optimization we used three different optimization algorithms in MATLAB, namely fmincon¹⁰⁷ (corresponding to O_1 in Fig. (18)), fminsearch¹⁰⁸ (O_2) (more precisely fminsearch with boundaries¹⁰⁹), and patternsearch¹¹⁰ (O_3). For the first constraint, C_1 , we attempt to avoid the discontinuities in P_T by first defining the following numerical derivatives:

$$\Delta P_{T,n,1,p} = \frac{P_T(r_n + \Delta r_1) - P_T(r_n)}{\Delta r_1} \quad (76)$$

$$\Delta P_{T,n,2,p} = \frac{P_T(r_n + \Delta r_2) - P_T(r_n)}{\Delta r_2} \quad (77)$$

$$\Delta P_{T,n,1,m} = \frac{P_T(r_n) - P_T(r_n - \Delta r_1)}{\Delta r_1} \quad (78)$$

$$\Delta P_{T,n,2,m} = \frac{P_T(r_n) - P_T(r_n - \Delta r_2)}{\Delta r_2}, \quad (79)$$

where we have used $\Delta r_1 = 1\text{ nm}$ and $\Delta r_2 = 0.5\text{ nm}$ and n corresponds to the parameters r_1 , r_2 or r_3 and so on. If either $|\Delta P_{T,n,1,p} - \Delta P_{T,n,2,p}|/P_0 > 15.34$ or $|\Delta P_{T,n,1,m} - \Delta P_{T,n,2,m}|/P_0 > 15.34$ then β is artificially put to 0 such that the optimization avoids this point. The condition is then tested for all the parameters r_n . In the second constraint, C_2 , we simply attempt to avoid all points where a new guided mode appears. Here we simply test if there is any difference in the number of guided modes within $\pm 0.5\text{ nm}$ of all the parameters. If this is the case $\beta = 0$.

10.9 Additional simulations of the photonic nanowire

Here we will present the reflections and transmission coefficients of the photonic nanowire. First, we will optimize the reflection of the fundamental mode, $R_{1,1} = |r_{1,1}|^2$, at the bottom mirror with respect to the silica layer thickness, t_{SiO_2} , which can reduce the coupling to surface plasmons and radiation modes^{81,82}.

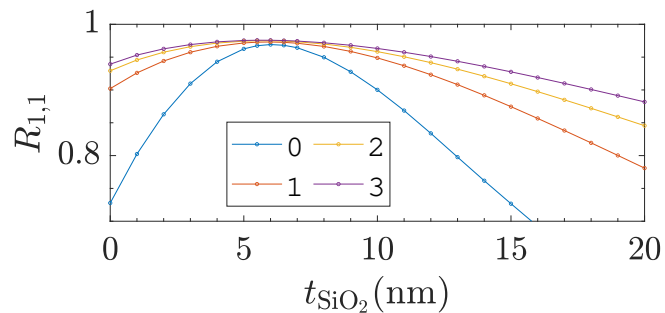


Fig. 19 The reflection of the fundamental mode, $R_{1,1}$, at the bottom interface as a function of the silica layer thickness, t_{SiO_2} , for 0, 1, 2 and 3 rings.

In Fig. (19) the reflection of the fundamental mode, $R_{1,1}$, is shown as a function of the silica layer thickness, t_{SiO_2} , for 0, 1, 2 and 3 rings. The silica layer thickness which provides the maximum reflection is close to $t_{\text{SiO}_2} = 6\text{ nm}$ for all numbers of rings. There is also a very slight increase in the maximum reflection as the numbers of rings increases, which is caused by the slightly increasing center diameter. The reflections at $t_{\text{SiO}_2} = 6\text{ nm}$ are: $R_{1,1,0} = 0.9692$, $R_{1,1,1} = 0.9731$, $R_{1,1,2} = 0.9749$ and $R_{1,1,3} = 0.9757$, where the last sub index refers to the numbers of rings. The total reflection, $R_{\text{total},1}$, which includes scattering into radiation modes and any ring modes are: $R_{\text{total},1,0} = 0.9694$, $R_{\text{total},1,1} = 0.9733$, $R_{\text{total},1,2} = 0.9751$ and $R_{\text{total},1,3} = 0.9758$ showing that an insignificant amount of the fundamental mode is back-scattered into radiation. We have thus chosen $t_{\text{SiO}_2} = 6\text{ nm}$.

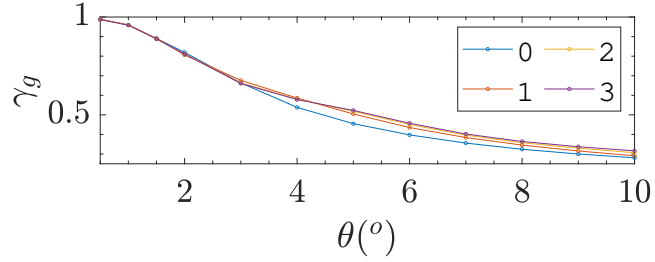


Fig. 20 The transmission coefficient with the Gaussian overlap, γ_g (NA = 0.75), as a function of the taper angle, θ , for the different numbers of rings.

In Fig. (20) the transmission coefficient with the Gaussian overlap, γ_g (NA = 0.75), is shown as a function of the taper angle, θ , for the different numbers of rings. The transmission coefficient is strongly dependent on the opening angle and so will the overall performance. For the smallest tapering angles, the transmission coefficient is almost the same for the different numbers of rings, which showcases that neither the increased diameter nor the rings decrease the transmission. The values obtained at $\theta = 0.5^\circ$ with NA = 0.75 are: $\gamma_{g,0} = 0.9884$, $\gamma_{g,1} = 0.9882$, $\gamma_{g,2} = 0.9877$ and $\gamma_{g,3} = 0.9870$. Around $\theta = 2^\circ$, the transmission is slightly better without any rings and then for $\theta \geq 4^\circ$ the transmission is slightly better with the rings which is caused by the diameter change. To show the influence of the numerical aperture, we also plot the transmission coefficient as a function of the NA for 1 ring.

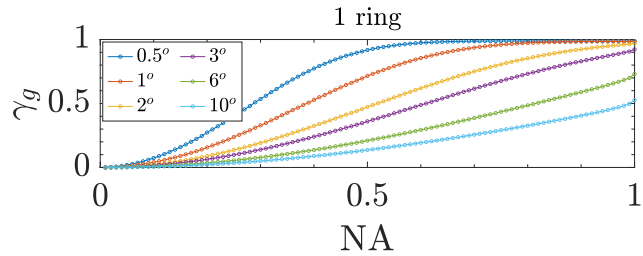


Fig. 21 The transmission coefficient with the Gaussian overlap, γ_g , for 1 ring as a function of the NA for a few different tapering angles θ .

In Fig. (21), the transmission coefficient with the Gaussian overlap, γ_g , is shown for 1 ring as a function of the NA, for a few different tapering angles θ . In general, a larger NA increases the transmission coefficient and the same is true for the tapering angle. For large values of NA, decreasing the tapering angle further than $\theta = 1^\circ$ does not increase the maximum transmission coefficient, but it does relax the requirement of the NA to obtain the maximum value.

With the decreased transmission coefficient, we expect an increased reflection at the top interface. The light can both be reflected back into the fundamental mode, but it can also be reflected back into radiation modes.

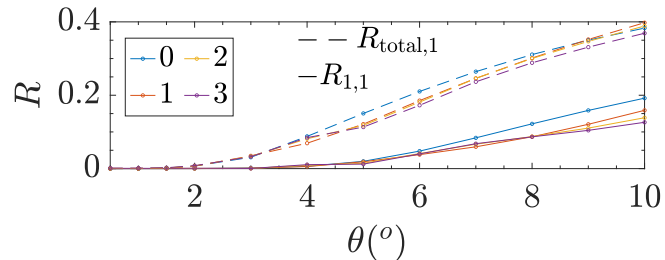


Fig. 22 The reflection of the fundamental mode into itself, $R_{1,1}$ (solid lines), and the total reflection of the fundamental mode, $R_{\text{total},1}$ (dotted lines), as a function of the tapering angle, θ , for the different numbers of rings.

In Fig. (22), the reflection of the fundamental mode into itself, $R_{1,1}$, and the total reflection of the fundamental mode, $R_{\text{total},1}$, is shown as a function of the tapering angle, θ , for the different numbers of rings. For tapering angles below 2° , the reflection is very small, but already at $\theta = 3^\circ$ the total reflection is around 0.03. Furthermore, most of the reflection is not into the fundamental mode itself, but into radiation modes and potentially ring modes. This also complicates the optimal values of h_b and h_t for the efficiency. Nonetheless, the reflection is very small for the lowest tapering angles.

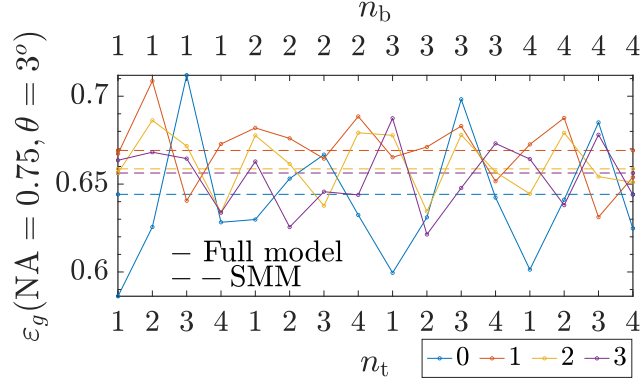


Fig. 23 Collection efficiency, ε_g (NA = 0.75), as a function of the 16 different combinations of n_b and n_t for the different numbers of rings at a tapering angle of $\theta = 3^\circ$. The dotted line is calculated using the SMM while the solid line is the full model.

In Fig. (23), the collection efficiency can vary up to 0.1 even when the tapering angle is only $\theta = 3^\circ$. This significantly benefits the structure without any rings as seen by comparing to the SMM. As such the effect of positioning the dipole dominates over the effect of the rings for larger tapering angles.

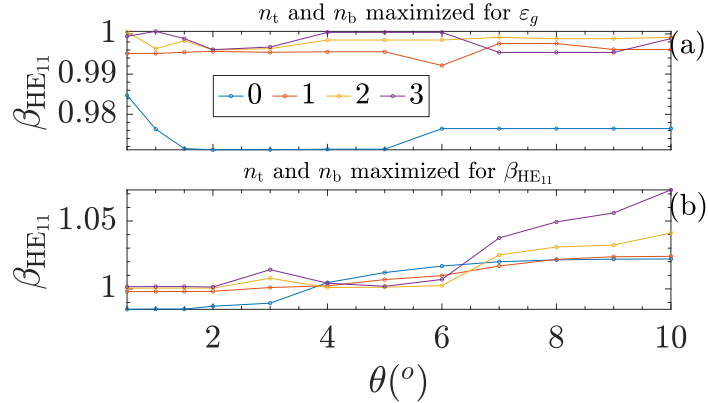


Fig. 24 $\beta_{HE_{11}}$ as a function of the tapering angle, θ , for the different numbers of rings where n_t and n_b are chosen such that (a) ε_g (NA = 0.75) is maximised or (b) $\beta_{HE_{11}}$ is maximised.

In Fig. (24), $\beta_{HE_{11}}$ is shown as a function of the tapering angle, θ , for the different numbers of rings where n_t and n_b are chosen such that (a) ε_g (NA = 0.75) is maximised and (b) $\beta_{HE_{11}}$ is maximised. In Fig. (24a), $\beta_{HE_{11}}$ is above 0.99 for any rings added and the value is close to the value for the infinite structures. $\beta_{HE_{11}}$ even slightly exceeds 1 for 2 and 3 rings due to coupling between the evanescent modes and the fundamental mode, which indicates the breakdown of the SMM. For the structure without any rings, there is an increase in $\beta_{HE_{11}}$ of at least 0.01 for all angles. If we then choose n_t and n_b such that $\beta_{HE_{11}}$ is maximised as in Fig. (24b), then $\beta_{HE_{11}}$ exceeds 1 for many tapering angles and even reaches 1.07 for 3 rings at $\theta = 10^\circ$. This is again due to a breakdown of the SMM which we have also reported in⁸² for the nanopost SPS. It also shows that maximizing $\beta_{HE_{11}}$ and ε_g is not the same due to this breakdown. However, in the infinite structure $\beta_{HE_{11}}$ is well-defined as a power ratio and as has already been shown is indeed useful when optimizing the collection efficiency.

10.10 Additional simulations of the Micropillar

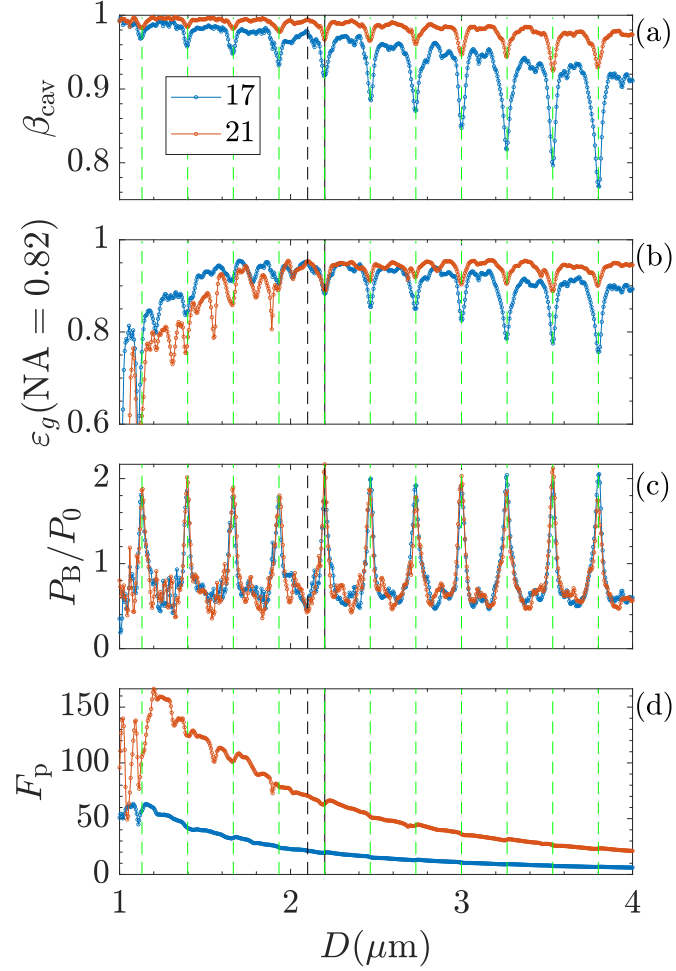


Fig. 25 (a) β_{cav} , (b) $\varepsilon_g(\text{NA} = 0.82)$, (c) P_B/P_0 , and (d) F_p as a function of the diameter, D , for $n_{\text{top}} = 17$ and $n_{\text{top}} = 21$ top DBR layer pairs respectively. The β factor here, $\beta_{\text{cav}} = P_{\text{cav}}/P_{\text{f}}$, is defined for the cavity mode which is almost identical to the fundamental mode¹⁷. The green dotted lines indicate the diameters where new guided modes appear in the infinite GaAs wire. The black dotted lines indicate $D = 2.1\mu\text{m}$ and $D = 2.2\mu\text{m}$ which are chosen to add rings. At $D = 2.2\mu\text{m}$, the black dotted line overlaps with one of the green lines.

In Fig. (25), we present the reproduced (a) β factor, (b) $\varepsilon_g(\text{NA} = 0.82)$, (c) P_B/P_0 , and (d) F_p of Ref.¹⁷ as a function of the diameter, D , for $n_{\text{top}} = 17$ and $n_{\text{top}} = 21$ top DBR layer pairs respectively. There are several peaks in the collection efficiency, both for $n_{\text{top}} = 17$ and $n_{\text{top}} = 21$ with values around $\varepsilon_g = 0.95$. There are also several dips as described in the main text of the paper. At $D = 2.1\mu\text{m}$, we obtain $\varepsilon_{g,17} = 0.9497$ and $\varepsilon_{g,21} = 0.9529$ and this is one diameter for which we have chosen to add rings. At $D = 2.2\mu\text{m}$, we obtain $\varepsilon_{g,17} = 0.8829$ and $\varepsilon_{g,21} = 0.8901$ and this is the other diameter for which we have chosen to add rings.

In Fig. (26), (a) β_{cav} with $n_{\text{top}} = 17$, (b) β_{cav} with $n_{\text{top}} = 21$, (c) $\varepsilon_g(\text{NA} = 0.82)$ with $n_{\text{top}} = 17$, and (d) $\varepsilon_g(\text{NA} = 0.82)$ with $n_{\text{top}} = 21$ are shown as a function of the air gap, r_1 , and the ring thickness, r_2 , for 2 rings with fixed parameters surrounding the structure. For $n_{\text{top}} = 17$, the pattern of β_{cav} and $\varepsilon_g(\text{NA} = 0.82)$ do agree very well with a slight deviation of the position for the maximum value. For $n_{\text{top}} = 21$, the agreement of the patterns is not as good, but still comparable. Ultimately, the collection efficiency can be increased from $\varepsilon_{g,17} = 0.9497$ to $\varepsilon_{g,17,2} = 0.9610$ at $r_1 = 0.13\mu\text{m}$ and $r_2 = 0.08\mu\text{m}$ and for $n_{\text{top}} = 21$ from $\varepsilon_{g,21} = 0.9529$ to $\varepsilon_{g,21,2} = 0.9581$ at $r_1 = 0.39\mu\text{m}$ and $r_2 = 0.05\mu\text{m}$.

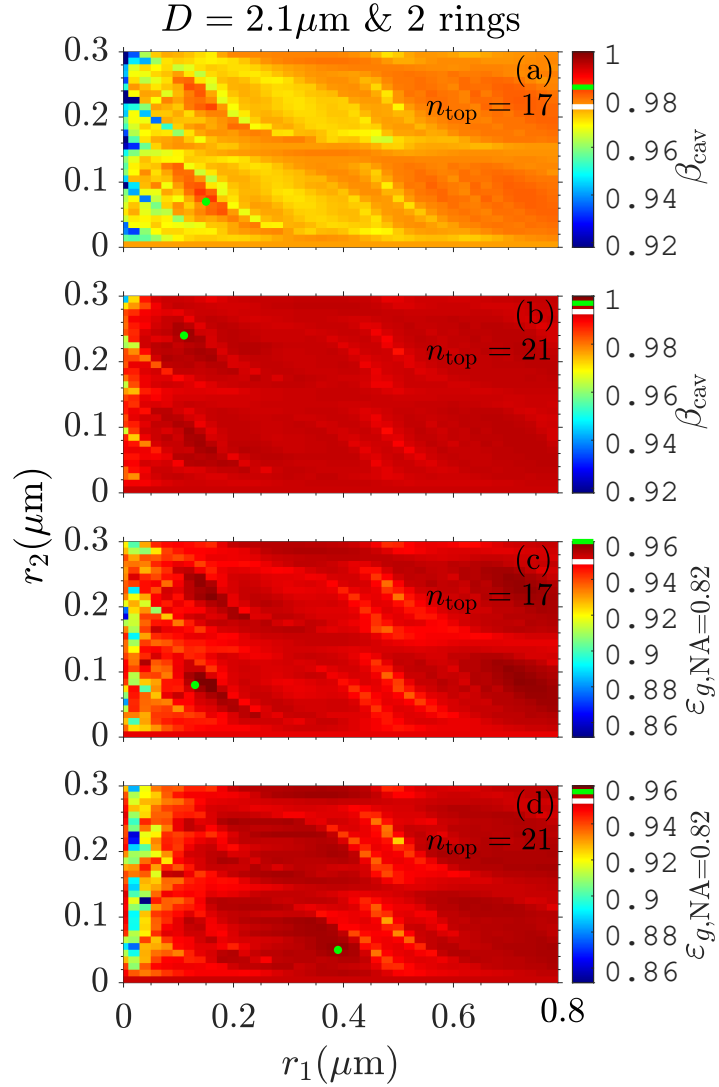


Fig. 26 (a) β_{cav} with $n_{\text{top}} = 17$, (b) β_{cav} with $n_{\text{top}} = 21$, (c) $\epsilon_g(\text{NA} = 0.82)$ with $n_{\text{top}} = 17$, and (d) $\epsilon_g(\text{NA} = 0.82)$ with $n_{\text{top}} = 21$ as a function of the air gap, r_1 , and the ring thickness, r_2 , for 2 rings at $D = 2.1\mu\text{m}$. The green dots indicate the maximum values without any restrictions. The white line in the colorbars indicates the value without a ring and the green line indicates the value at the green dot. Note: a few of the darkest blue data points have lower values than indicated by the color bars, but the limit is chosen to increase the visibility.